



Modeling Dust Production, Growth, and Destruction in Reionization-era Galaxies with the CROC Simulations. II. Predicting the Dust Content of

Downloaded from: <https://research.chalmers.se>, 2024-07-17 16:26 UTC



Citation for the original published paper (version of record):

Esmerian, C., Gnedin, N. (2024). Modeling Dust Production, Growth, and Destruction in Reionization-era Galaxies with the CROC Simulations. II. Predicting the Dust Content of High-redshift Galaxies. *Astrophysical Journal*, 968(2). <http://dx.doi.org/10.3847/1538-4357/ad410f>

N.B. When citing this work, cite the original published paper.



Modeling Dust Production, Growth, and Destruction in Reionization-era Galaxies with the CROC Simulations. II. Predicting the Dust Content of High-redshift Galaxies

Clarke J. Esmerian^{1,2,3,4}  and Nickolay Y. Gnedin^{1,2,3} ¹ Department of Astronomy & Astrophysics, University of Chicago, Chicago, IL 60637, USA; clarke.esmerian@gmail.com² Kavli Institute for Cosmological Physics; The University of Chicago; Chicago, IL 60637, USA³ Fermi National Accelerator Laboratory, Batavia, IL 60510, USA⁴ Department of Space, Earth, & Environment, Chalmers University of Technology, Chalmersplatsen 4, Gothenburg SE-412 96, Sweden

Received 2023 August 21; revised 2024 March 23; accepted 2024 April 19; published 2024 June 18

Abstract

We model the interstellar dust content of the reionization era with a suite of cosmological, fluid-dynamical simulations of galaxies with stellar masses ranging from $\sim 10^5$ to $10^9 M_\odot$ in the first 1.2 Gyr of the Universe. We use a post-processing method that accounts for dust creation and destruction processes, allowing us to systematically vary the parameters of these processes to test whether dust-dependent observable quantities of galaxies at these epochs could be useful for placing constraints on dust physics. We then forward model observable properties of these galaxies to compare to existing data. We find that we are unable to simultaneously match existing observational constraints with any one set of model parameters. Specifically, the models that predict the largest dust masses $D/Z \gtrsim 0.1$ at $z = 5$ —because of high assumed production yields and/or efficient growth via accretion in the interstellar medium—are preferred by constraints on total dust mass and infrared (IR) luminosities, but these models produce far too much attenuation in the ultraviolet (UV), preventing them from matching observations of β_{UV} . To investigate this discrepancy, we analyze the relative spatial distribution of stars and dust as probed by IR and UV emission, which appear to exhibit overly symmetric morphologies compared to existing data, likely due to the limitations of the stellar feedback model used in the simulations. Our results indicate that the observable properties of the dust distribution in high redshift galaxies are a particularly strong test of stellar feedback.

Unified Astronomy Thesaurus concepts: [Hydrodynamical simulations \(767\)](#); [Galaxy formation \(595\)](#); [Cosmology \(343\)](#); [Astronomical simulations \(1857\)](#)

1. Introduction

The successful launch and commissioning of JWST has begun a new era in astrophysics. Its unprecedented sensitivity to the emission of high-redshift ($z \gtrsim 5$) galaxies has already enabled the rapid accumulation of data on the earliest galaxies. The amount and properties of interstellar dust in these galaxies has a fundamental impact on observations across the entire electromagnetic spectrum, and consequently plays a central role in the understanding of this groundbreaking new data.

Motivated by this, we have developed a model for the evolution of dust in simulated high-redshift galaxies. Described in Esmerian & Gnedin (2022), we post-process simulations from the Cosmic Reionization on Computers project (CROC; Gnedin 2014, 2016; Gnedin & Kaurov 2014) with a model that determines the fraction of heavy elements in the interstellar medium (ISM) locked in solid dust grains accounting for their nucleation in the ejecta of asymptotic giant branch (AGB) stars and supernovae (SNe), their growth via accretion of gas-phase metals in the cold molecular ISM, and their destruction via thermal sputtering due to hot gas from supernova remnants (SNRs). Since the rates of each of these processes are very uncertain due to uncertainties in the material properties of dust grains, the mathematical terms describing them are parameterized with uncertainty factors that enable the exploration of the wide range of theoretical possibilities.

This model is calculated along Lagrangian tracers that sample gas dynamical quantities along pathlines for a representative fraction of the gas in Lagrangian regions of galaxies. This post-processing technique enables the exploration of dust models with a wide range of parameter choices, of course at the expense of some realism because dust effects are not calculated during simulation run time. In Esmerian & Gnedin (2022), we explored the full parameter space of the model by focusing on a single massive galaxy ($M_{\text{vir}} \sim 10^{11} M_\odot$, $M_* \sim 10^9 M_\odot$ at $z = 5$) and the interplay of different dust physical processes in a fully dynamic ISM. We found that reasonable parameter choices for the dust model predicted dust contents and dust-sensitive observables broadly consistent with the extant observational constraints.

For purposes of computational feasibility, this method development was done using the single most massive galaxy in a $10h^{-1}$ cMpc cosmological volume. However, because the initial conditions of large-scale structure are Gaussian random fields, galaxies form in dark matter halos with a wide range of masses and formation histories, which we know to fundamentally impact galaxy properties (see Behroozi et al. 2009, for contemporary constraints). Theoretical efforts must therefore strive to make predictions for halos that sample the distributions of masses and formation histories as completely as possible, in order to make predictions for the galaxy population in the real Universe.

This modeling is especially urgent given the recent onslaught of data from JWST, coupled with ambitious programs using radio telescope arrays such as the Atacama Large Millimeter/submillimeter Array (ALMA), that are rapidly fleshing out the



Original content from this work may be used under the terms of the [Creative Commons Attribution 4.0 licence](#). Any further distribution of this work must maintain attribution to the author(s) and the title of the work, journal citation and DOI.

properties of the high-redshift galaxy population. Some of the most exciting and puzzling results from this recent revolution have implicated cosmic dust in a central role. There are exciting claims of anomalously bright galaxies and a surprisingly high star formation rate density at $z > 10$ abound (see Bouwens et al. 2023, and references therein), although these are dependent on photometric candidate detections without spectroscopic confirmation and therefore subject to possible revision. If confirmed, reconciling these with the mainstream galaxy formation models may present a challenge, and the many uncertainties of dust enrichment in the first galaxies have been invoked as possible explanations (Ferrara et al. 2023; Mason et al. 2023; Mirocha & Furlanetto 2023). Galaxies with spectroscopic confirmation rest on surer footing, and thus far all show evidence for little dust attenuation ($z \gtrsim 10$; Arrabal Haro et al. 2023a, 2023b; Bunker et al. 2023; Curtis-Lake et al. 2023; Roberts-Borsani et al. 2023; Tacchella et al. 2023).

Nonetheless, the reionization epoch is anything but dust-free. ALMA programs REBELS (Bouwens et al. 2022; Inami et al. 2022) and ALPINE (Le Fèvre et al. 2020) and others (Bowler et al. 2022) have detected thermal dust continuum emission that firmly establishes significant amounts of dust in at least some galaxies by $z = 5\text{--}7$ (Fudamoto et al. 2020; Pozzi et al. 2021; Algera et al. 2023; Barrufet et al. 2023). These observations also hint at complicated dust morphologies with significant spatial displacement from the stellar component (Bowler et al. 2022; Inami et al. 2022). Additionally, Rodighiero et al. (2023) presented an analysis of JWST candidate detections that suggest significant dust obscuration at $8 < z < 13$. Overall, there is convincing evidence for the very rapid buildup of dust during the reionization epoch, especially in the most massive galaxies. Models of galaxy formation will therefore need to account for the physics of dust if they are to satisfactorily explain key observable constraints on cosmic dawn.

With this goal, in this paper we now extend our previous analysis by applying our dust modeling framework to a suite of 10 additional simulated galaxies from the same simulation volume, selected with approximately uniform logarithmic spacing in final halo mass $1.1 \times 10^9 M_\odot \leq M_{\text{vir}} \leq 5.0 \times 10^{11} M_\odot$, corresponding to stellar masses $3.7 \times 10^5 M_\odot \leq M_* \leq 1.9 \times 10^9 M_\odot$, allowing us to assess the dependence of our predicted dust properties on galaxy mass at a given cosmological time. The paucity of dust at cosmic dawn suggested by some observations motivates us to also explore a wider range of dust modeling choices, namely those that either produce less dust or destroy it more efficiently. Section 2 explains our simulated galaxy sample selection, notes small updates to the methodology presented in the first paper, and presents the dust model variations explored in this analysis. Section 3 presents the galaxy mass–metallicity relation predicted by the simulations compared to existing high-redshift constraints, and results of the dust model applied to our simulated galaxy sample. Specifically, we present the predicted dust content and dust-sensitive observable quantities, both galaxy-averaged and spatially resolved, to which we compare to existing data. Section 4 discusses the agreements and discrepancies between our model predictions and observational constraints, and compares our work to other recent similar investigations in the literature. We conclude in Section 5.

2. Methods

2.1. CROC Simulation

The galaxy formation simulation model, halo identification, and galaxy definitions are identical to those described in Esmerian & Gnedin (2022), to which we refer the reader. For this paper’s analysis, we select a total of 11 galaxies from a $10h^{-1}$ comoving Megaparsec (cmMpc) cosmological volume with final $z=5$ halo masses $1.1 \times 10^9 M_\odot \leq M_{\text{vir}} \leq 5.0 \times 10^{11} M_\odot$, corresponding to final stellar masses $3.7 \times 10^5 M_\odot \leq M_* \leq 1.9 \times 10^9 M_\odot$. These limits span the range of halo masses resolved in the simulation. The 11 halos are selected with approximately logarithmically uniform spacing in final halo mass. Since the galaxy scaling relations predicted by CROC have small scatter (see Zhu et al. 2020 and Noel et al. 2022) and do not dramatically change slope on scales $\lesssim 0.5$ dex in halo mass, it is sufficient for the purposes of this analysis to sample one halo of a given mass with the average spacing of 0.24 dex provided by a total sample of 11. This simulation has the same initial conditions as the one used in the previous paper, so the most massive halo is the same.

2.2. Lagrangian Tracer Sampling and Dust Model

As in the previous paper, we take as input to our dust model the ISM conditions in our simulated galaxies sampled along pathlines obtained with Lagrangian tracer particles—i.e., particles that follow the fluid flow predicted by the gas dynamics solver used in the simulation. These particles are initialized in random positions (weighted by the local gas density) in the Lagrangian region of the halo and follow the fluid flow using the Monte-Carlo method introduced in Genel et al. (2013) and implemented in the ART code in Semenov et al. (2018). The number of tracers per halo scales with halo mass such that the minimum number of tracers for a given halo is above 100. For galaxies hosted in halos with final masses $M_{\text{vir}} > 10^{11} M_\odot$, we downsample to 10^4 particles for computational feasibility.

Along each pathline, we sample the quantities predicted by the simulation as a function of time: gas number density n , gas temperature T , gas-phase metallicity Z , neutral hydrogen fraction f_{HI} (calculated with the on-the-fly radiative transfer based on stellar sources as described in Gnedin 2014), and molecular hydrogen fraction f_{H_2} (calculated based on the fitting function from Gnedin & Draine 2014). Along these pathlines, tracers also record the local rates of metal enrichment due to SN and AGB winds \dot{Z}_{SN} and \dot{Z}_{AGB} and number density of SN explosions \dot{n}_{SN} based on the metallicity and age of the star particles in the same computational cell. These quantities are sufficient to calculate the rates of change in the dust-to-gas ratio \dot{D} based on our dust physics model. The physical processes included in the model are as follows:

1. Production: a constant fraction of metals returned to the ISM by SNe and AGB stars are assumed to nucleate in these ejecta and enter the ISM as dust grains. These yields are separate for the two processes y_{SN} and y_{AGB} , so they can be varied independently. Default values of 0.1 are adopted based on Dwek (1998).
2. Growth: dust grains are allowed to grow in the dense ISM by the accretion of gas-phase metals, with a characteristic growth timescale τ_{accr} . The expression from this rate is derived from the two-body collision rate between atoms

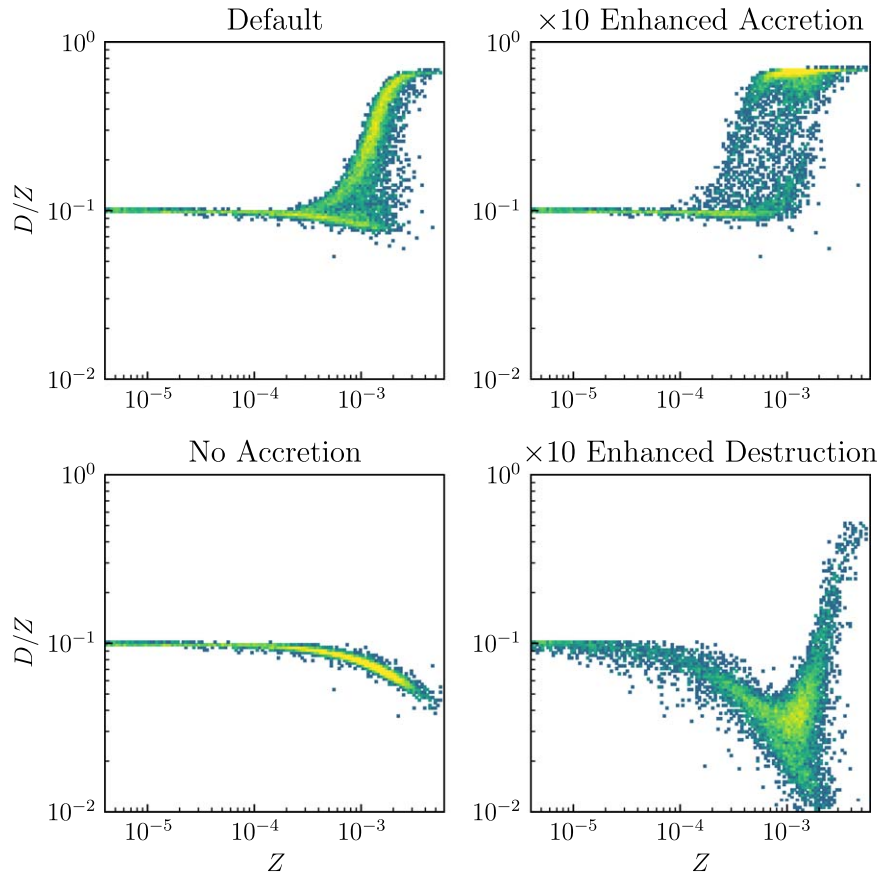


Figure 1. Spatially resolved D/Z vs. Z relations. Each panel shows the 2D PDF of mass for D/Z vs. Z in the ISM of the most massive galaxy at the last snapshot. Different panels correspond to different dust models.

in the gas phase and dust grains (Draine 1990; Dwek 1998; Weingartner & Draine 1999; Feldmann 2015).

3. Destruction: dust grains are destroyed in the shocks and hot gas produced by SNRs, assuming each SN sweeps out a given mass of ISM with a destruction efficiency taken from McKee (1989).

These processes define a pair of coupled ordinary differential equations for the evolution of the dust-to-gas ratio D and metallicity Z_{tracer} that can be integrated in post-processing to predict the dust content along each sampled trajectory in the simulation. Note that the metallicity accumulated by the tracer is not necessarily identical to the metallicity of the gas it samples due to the stochasticity of stellar enrichment events and our inability to account for advection near pathlines, which is why we use a separate symbol for it. With this information, for every computational cell in the simulation sampled by a tracer, we can calculate its dust mass as $(D/Z_{\text{tracer}}) Z_{\text{simulation}} M_{\text{gas, cell}}$.

Computational resource limitations prevent us from using enough tracers that all cells in each galaxy are sampled. Consequently, we must find a way to assign dust masses to cells in the galaxy that were not sampled by any tracer. To do this, we interpolate the D/Z versus Z relation for the tracers in each galaxy at every snapshot output. As shown in Figure 1, the dust-to-metal ratio scales regularly with metallicity, making this interpolation the best option for assigning dust masses to unsampled cells in a way that preserves the predictions of the dust model. We note that with some model choices even this relation exhibits significant scatter at a given tracer metallicity.

Our correction therefore possibly underestimates the scatter in observable quantities impacted by the dust distribution.

We note that in Esmerian & Gnedin (2022) we had not yet realized this correction was necessary, and therefore the results in that paper underestimate the total dust mass and effect of dust on observable quantities. These effects are $\mathcal{O}(10\%)$ in the dust mass but can be order-unity for some observable quantities that depend sensitively on the dust distribution—particularly dust attenuation of ultraviolet (UV) starlight—but do not change the qualitative conclusions of that paper.

As acknowledged in Esmerian & Gnedin (2022), this post-processing method is, in principle, inferior to a fully coupled treatment of dust on-the-fly in the simulations. Post-processing fundamentally cannot account for the dynamical effects of dust on the gas dynamics or radiative transfer in the simulation. It is necessitated by computational constraints that would totally prohibit the parameter exploration, which is a central goal of our investigation. However, we believe it to be adequate for the following reasons: (1) The galaxy formation model in CROC is tuned to match the observed high-redshift UV luminosity function and reionization history of the intergalactic medium (Gnedin 2014, 2016), and it is quite likely that any change to the simulation resulting from dust dynamical effects could be eliminated by a similar change in the parameters of the simulation’s star formation prescription. (2) Arguably the most important dynamical effect of dust would be its change to the radiative cooling rates of gas in the simulation (dust removes heavy elements from the gas phase, which cause metal line cooling, and itself is a source of both photoelectric heating and

cooling due to IR emission), but these rates are not known to better than a factor of a few even in principle (see, e.g., Gnat & Sternberg 2007; Wiersma et al. 2009), so the more sophisticated modeling of dust that would change cooling rates by similar or smaller values would not necessarily have higher physical fidelity. (3) The dynamical effects of dust would likely depend on the structure and dynamics of gas flows on scales unresolved (i.e., $\lesssim 100$ pc) in the ISM of our simulations.

2.3. Forward-modeling Unresolved Galaxy Observable Quantities

The methods used to calculate dust-dependent observables (the effective optical depth to dust at 1500 \AA : τ_{1500} , the logarithmic spectral slope in the UV: β_{UV} , the infrared (IR) luminosity: L_{IR} and the infrared excess $\text{IRX} \equiv L_{\text{IR}}/L_{\text{UV}}$) are identical to the description in Esmerian & Gnedin (2022), which we summarize here for completeness. With the spatial distribution of dust for an entire simulated galaxy obtained as described above, we calculate the dust column densities to every star particle along six lines of sight (the three coordinate axes in both directions), which uniformly sample all possible observation orientations and are random with respect to the galaxy geometry. We can therefore assign a wavelength-dependent optical depth to each star particle using the mass absorption coefficient from the SMC bar model of Weingartner & Draine (2001). To calculate rest-frame UV observables, to each star particle we assign a stellar spectrum from the Flexible Stellar Population Synthesis code (Conroy & Gunn 2010) based on the star particle age and metallicity—quantities that are predicted by the simulation. These are then extinguished based on the dust optical depth calculated from the column density assuming the dust opacity law from Weingartner & Draine (2001, SMC model⁵). The extinguished spectra from all star particles in a galaxy combined define the galaxy’s UV and optical spectrum. The galaxy’s UV luminosity L_{UV} is defined at $\lambda = 1500 \text{ \AA}$ and β_{UV} is calculated as the logarithmic slope of the best-fitting power law to the galaxy spectrum (i.e., $f_{\lambda} \propto \lambda^{\beta_{\text{UV}}}$ using the UV wavelength bands defined in Calzetti et al. 1994 to avoid contamination by absorption features).

We note that this calculation only accounts for line-of-sight extinction and does not account for the geometric effects of scattering. While this simplification may impact our predicted UV observables quantitatively because the dust albedo is potentially nonnegligible at these wavelengths (it is approximately 0.4 at 1500 \AA in the dust opacity model we employ), we do not anticipate it would qualitatively change our results. As we demonstrate in our analysis of the spatially resolved properties of our dust model predictions in Section 3.4, the UV properties of these galaxies are primarily determined by lines of sight that have either negligible dust extinction—in which case the contribution from scattering is also negligible—or such high optical depths that the ISM is effectively opaque in the UV—in which all of the UV light would be absorbed before escaping to be scattered into our mock observations. Moreover, this spatial analysis also demonstrates that the low resolution of our simulated galaxies likely fails to capture a realistically dynamic and porous ISM, and thus the effects of dust scattering

(which depend strongly on dust geometry) are unlikely to be reproduced either.

The rest-frame IR luminosity from each cell is calculated as a modified blackbody (i.e., in the optically thin limit) $L_{\lambda} = 4\pi M_D \kappa_D B_{\lambda}(T_D)$ where M_D is the dust mass, κ_D is the same SMC (Weingartner & Draine 2001) opacity law assumed for the UV quantities, and $B_{\lambda}(T_D)$ is a blackbody of dust temperature T_D . Since the calculation of the dust temperature is extremely complicated and relies on many other uncertain parameters such as the material properties of the dust grains (see, e.g., Lower et al. 2024), we simply assume $T_D = 40 \text{ K}$ throughout. See Esmerian & Gnedin (2022) for the effects of varying this parameter.

2.4. Spatially Resolved Images

For the analysis of spatially resolved dust properties, we focus exclusively on the most massive galaxy in the simulation, which attains a stellar mass of $M_* = 1.3 \times 10^8 M_{\odot}$ by $z = 8$, $M_* = 7.1 \times 10^8 M_{\odot}$ by $z = 6.4$ and $M_* = 1.9 \times 10^9 M_{\odot}$ by $z = 5$. Our simulated galaxy is therefore well within the range of stellar masses probed by observations to which we compare (Inami et al. 2022), justifying comparison because galaxy morphology is expected to depend on stellar mass (Pillepich et al. 2019). However, we note that for these snapshots it has a much lower SFR of $\lesssim 5.2 M_{\odot} \text{ yr}^{-1}$ than any galaxy in this sample. This may be due to the bias toward high SFR systems of these observations noted in Section 1, or the inability of the CROC model to produce such rapidly star-forming systems. Figure 6 of Zhu et al. (2020) shows that the CROC galaxies exhibit small scatter in the SFR–stellar mass relationship, suggesting that the discrepancy between our simulation’s SFR and those inferred from data results from a deficiency of the model and would not be alleviated by considering a larger number of simulated galaxies. This discrepancy provides further motivation to compare our simulations to data in a spatially resolved analysis, as this may provide information about the cause of these discrepancies.

We present results for this simulation at 12 snapshots from $z = 8.5$ to $z = 5$. The upper bound in redshift is motivated by the upper bound on the observations, but we include snapshots lower than the observational lower bound of $z = 6.5$ to maximize the galaxy mass range probed by our analysis. We note that we have redone the analysis restricted to only snapshots within $6.4 < z < 8.5$, identical to the observations, and all of our conclusions are unchanged. We also note that based on visual inspection, the galaxy undergoes merging events at $z \approx 7.3$ and $z \approx 6$, which significantly disrupt its morphology. There are enough snapshots of the simulation that the galaxy morphology before, during, and after the merger event can be clearly distinguished. We therefore expect that our simulation data samples a sufficiently violent merger history with sufficiently high time resolution that our analysis accounts for the morphological effects of accretion history on high-redshift galaxies of the relevant masses.

This spatial analysis uses quantities calculated as described previously except with small modifications. UV colors are determined based on the finite difference between luminosities at 1500 and 2500 \AA as follows:

$$\beta_{\text{UV}} = \frac{\log_{10}(f_{2500 \text{ \AA}}/f_{1500 \text{ \AA}})}{\log_{10}(2500 \text{ \AA}/1500 \text{ \AA})} \quad (1)$$

⁵ Obtained from https://www.astro.princeton.edu/~draine/dust/extcurvs/kext_albedo_WD_SMCbar_0.

Model Name	Key Parameters	Description	Color in Figures
Default	$y_{D,SN} = y_{D,AGB} = 0.1,$ $\tau_{\text{accr}} = 3 \times 10^8 \text{ yr}, C_{\text{dest}} = 1$	Default from Esmerian & Gnedin (2022), parameters based on Dwek (1998); Feldmann (2015).	●
No Accretion	$\tau_{\text{accr}} = \infty$	No grain growth due to gas-phase accretion in cold ISM	●
Enhanced Accretion	$\tau_{\text{accr}} = 0.1\tau_{\text{accr,Default}}$	Enhanced grain growth due to gas-phase accretion in cold ISM	●
No Destruction	$C_{\text{dest}} = 0$	No grain destruction in hot gas due to SNRs	●
Enhanced Destruction	$C_{\text{dest}} = 10C_{\text{dest,Default}}$	Enhanced grain destruction in hot gas due to SNRs	●
Very Enhanced Destruction	$C_{\text{dest}} = 100C_{\text{dest,Default}}$	Very enhanced grain destruction in hot gas due to SNRs	●
Low SN Production	$y_{D,SN} = 0.1y_{D,SN,Default}$	Suppressed dust yield from SN	●
No SN Production	$y_{D,SN} = 0$	SN do not produce dust	●
Very Low SN Production, No AGB Production	$y_{D,SN} = 0.1y_{D,SN,Default},$ $y_{D,AGB} = 0$	Very suppressed dust yield from SN, AGB do not produce dust	●

Figure 2. Explored parameter combinations. Note that for each model, any parameter not listed under Key Parameters is the same as the Default model.

again on an individual star particle basis. We note that this is not identical to the calculation of β_{UV} in the rest of the analysis, in which a least-squares fit was performed on this portion of the UV spectrum to determine a power-law slope. This finite difference method is adopted for computational ease, and we have checked that it reproduces the least-squares fitting results very accurately.

We use dust column density Σ_D , computed from the galaxy dust mass distribution calculation as a proxy for IR continuum emission. The two are directly proportional because the dust distribution is optically thin in the IR.

To account for the effect of finite observational resolution, we smooth with a Gaussian kernel with variance $\sigma^2 = \frac{\Delta_{\text{FWHM}}^2}{8 \ln 2}$ where Δ_{FWHM} is the physical distance at the simulation snapshot redshift corresponding to the angular FWHM of the observation. We explore Δ_{FWHM} values of 0''2 and 0''8, which for the redshift range of our simulations $11.4 \geq z \geq 5.0$ corresponds to a physical size of 0.33–0.55 kpc and 1.32–2.19 kpc, respectively.

2.5. Dust Model Parameter Exploration

As in the previous paper, we run a suite of dust models with different parameter choices to explore their impact on the predicted dust content of high-redshift galaxies and dependent observables, now on a sample of multiple simulated galaxies. However, motivated by observations that increasingly point to minimal dust in the earliest galaxies (e.g., Roberts-Borsani et al. 2023; Tacchella et al. 2023), we extended the set of parameter variations explored by introducing three new models that either increase the grain destruction rate in SNRs (very enhanced destruction) or decrease grain production in SNe and/or AGBs (no SN production, and very low SN production, no AGB production). The list of models explored in this analysis is summarized in Figure 2 and described below. Note that each model is assigned a unique color for Figures 5–10 and 12, which are shown in the rightmost column of the table.

1. *Default*: This is identical to the “Default” model explored in Esmerian & Gnedin (2022), for which parameters were chosen to be the same as successful similar physical models of dust evolution for local-Universe galaxies (Dwek 1998; Feldmann 2015; Li et al. 2019).
2. *No Accretion*: This is identical to the “No Accretion” model in Esmerian & Gnedin (2022). The parameters of this model are identical to Default, except that grain

growth due to accretion of gas-phase metals in the cold molecular ISM is not allowed. This parameter choice is motivated by arguments based on microphysical considerations of dust grain geometry that grain growth in the cold phase of the ISM may not be possible (Ferrara et al. 2016).

3. *Enhanced Accretion*: This is identical to the “Enhanced Accretion” model in Esmerian & Gnedin (2022). The parameters of this model are identical to Default, except that grain growth due to accretion of gas-phase metals in the cold molecular ISM is enhanced by an order of magnitude. This parameter choice is motivated both by uncertainties in the unresolved density distribution of the cold ISM in our simulations, where grain growth is expected to be most efficient, and to enable comparison to other works that adopt faster grain growth rates (Graziani et al. 2020; Lewis et al. 2023).
4. *No Destruction*: This is identical to the “No Destruction” model in Esmerian & Gnedin (2022). The parameters of this model are identical to Default, except that grain destruction in the hot gas of SNRs is not allowed. This parameter choice is motivated by indirect observational indications of inefficient dust destruction in high-temperature gas (Gall & Hjorth 2018; Gjergo et al. 2018; Michałowski et al. 2019; Vogelsberger et al. 2019), as well as uncertainties in the unresolved ISM phase structure in our simulations.
5. *Enhanced Destruction*: This is identical to the “Enhanced Destruction” model in Esmerian & Gnedin (2022). The parameters of this model are identical to Default, except that grain destruction in the hot gas of SNRs is enhanced by an order of magnitude. This parameter choice is motivated by uncertainties in the destruction efficiency of individual SNRs both due to the microphysics of dust and unresolved ISM phase structure (McKee 1989; Hu et al. 2019; Kirchschrager et al. 2022).
6. *Very Enhanced Destruction*: The parameters of this model are identical to Default, except that grain destruction in the hot gas of SNRs is enhanced by two orders of magnitude. The motivation for this parameter choice is the same as for Enhanced Destruction, since the associated uncertainties are large, and also the increasing evidence for dust-free early galaxies as mentioned previously.
7. *Low SN Production*: Identical to Default, except that the dust yield from SNe is suppressed by an order of

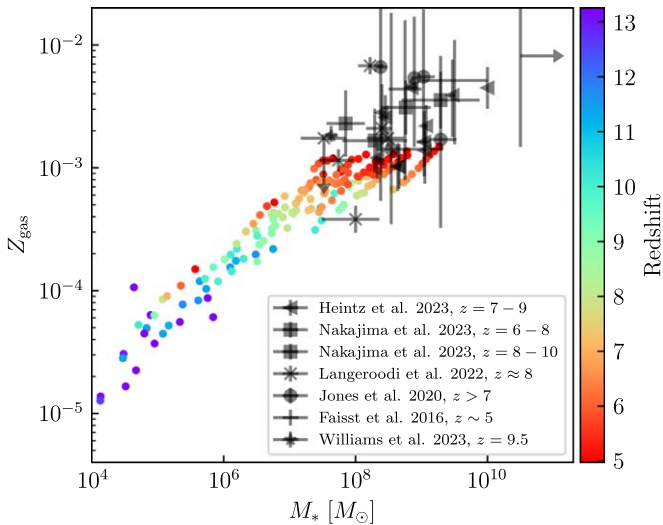


Figure 3. Mass–metallicity relation. The galaxy-averaged gas-phase metallicity is shown as a function of stellar mass. Each point represents an individual galaxy at an individual snapshot, colored by redshift. Observational data from galaxies at similar redshifts are from Faisst et al. (2016), Jones et al. (2020), Langeroodi et al. (2023), Nakajima et al. (2023), Heintz et al. (2023), and Williams et al. (2023) converted to mass fraction using $12 + [\text{O}/\text{H}]_{\odot} = 8.71$ and $Z_{\odot} = 0.02$ (Lodders 2019).

magnitude (i.e., $y_{D,\text{SN}} = 0.01$). Note that we do not change the AGB yield $y_{D,\text{AGB}}$, and since the AGB metal production is about 10 times smaller than that of SN (see Esmerian & Gnedin 2022, Figure 7), SN and AGB production are comparable with these parameters. This parameter choice is also motivated by the evidence for minimally dusty high-redshift galaxies, and uncertainties about the fraction of SN-produced dust that survives the reverse shock (see, e.g., Bianchi & Schneider 2007; Micelotta et al. 2016; Slavin et al. 2020).

8. *No SN Production:* Identical to Default but SN production is turned off— $y_{D,\text{SN}} = 0$. This choice is motivated by the extreme scenario in which no dust survives the reverse shock of any SNe.
9. *Very Low SN Production, No AGB Production:* Identical to Default, except that the dust yield from SNe is suppressed by two orders of magnitude (i.e., $y_{D,\text{SN}} = 10^{-3}$) and AGB production is turned off ($y_{D,\text{AGB}} = 0$). This is motivated by the same considerations as for the previous two models, and the deep uncertainties around AGB dust production, especially in the early Universe (e.g., Valiante et al. 2009; Schneider et al. 2014; Dell’Agli et al. 2019; Tosi et al. 2023).

3. Results

3.1. The Mass–Metallicity Relation

The dust content of galaxies is normalized by their overall metal content, so we first examine the galaxy metallicities in the simulations. Figure 3 shows the mass–metallicity relation for our simulations, including existing data at relevant redshifts. While the data mainly overlap with only the highest-mass galaxies in our sample, where there is overlap we see fair agreement, albeit with some indications of systematically low metallicities in CROC. The galaxy scaling relations of other quantities predicted by CROC have been thoroughly discussed and compared to existing data in

Zhu et al. (2020). We note that Noel et al. (2022) presented a more detailed analysis of the CROC mass–metallicity relation, but at the time these high-redshift data were not available for comparison, making this a new result.

3.2. The Dust Content of High-redshift Galaxies

The dust content of our simulated galaxies predicted by the models described in Section 2.5 and Figure 2 are summarized in Figure 4, where we show the galaxy-averaged dust-to-metal ratio D/Z as a function of galaxy metallicity Z in mass-fraction units (i.e., in which the average metallicity in the solar neighborhood is $Z_{\odot} = 0.02$). The top row shows the Default model and variations in the ISM grain growth accretion timescale. The middle row shows variations in the grain destruction efficiency of SNRs. And the bottom row shows variations in the assumed yields of dust production sources.

Broadly, we notice several trends. A well-established property of dust models similar to ours is the transition of dominant physical processes between low- and high-metallicity regimes: the D/Z ratio at low metallicity ($Z \lesssim 4 \times 10^{-4} = 2 \times 10^{-2} Z_{\odot}$) is primarily set by the choice of source yields $y_{D,\text{SN}/\text{AGB}}$, while the ratio at high metallicity is determined by a competition between the timescale for grain growth due to accretion in the ISM, and the efficiency of grain destruction in the hot ionized medium. If grain growth dominates (as in Default, Enhanced Accretion, No Destruction, Low SN Production, No SN Production, and Very Low SN, No AGB), the D/Z ratio rises with increasing metallicity, while when destruction dominates (No Accretion, Enhanced Destruction, Very Enhanced Destruction), the opposite scaling is observed.

However, we note that in some models there is substantial scatter between galaxies even at fixed metallicity, particularly for those models where accretion dominates at late times. The efficiency of grain growth via accretion must therefore depend on galaxy properties beyond average metallicity, an effect not captured in simpler one-zone models (e.g., Feldmann 2015). For the Default and Enhanced Accretion models, we notice substantial scatter in the metallicity at which each galaxy enters the growth-dominated regime of rising D/Z .

Indeed, we note that the most massive galaxy in our sample exhibits rising D/Z at high metallicities in all models except No Accretion (where $D/Z > y_D$ is physically impossible) and Very Enhanced Destruction. Even in the Enhanced Destruction scenario, the D/Z ratio rises at late times (i.e., high metallicities) for this single galaxy but no others. This clearly indicates the importance of some combination of star formation history and ISM phase structure in setting the dominant dust regulating mechanisms. Precise determination of this cause would require more analysis beyond the scope of this work but would be interesting for future investigation.

Finally, we note the significant scatter in D/Z at very low metallicities ($Z \lesssim 10^{-4}$). As indicated by their redshift (indicated in color) and the stellar mass–metallicity relation in Figure 3, these low-metallicity galaxies are the highest-redshift and lowest-mass in our sample. Consequently, there are the most poorly resolved and subject to the greatest stochasticity effects from the discreteness of enrichment from star particles and sampling by Lagrangian tracers. The latter would be amended by coupling the dust model explicitly to the simulation, and is therefore another motivation for more sophisticated modeling in future analyses. Nonetheless, this

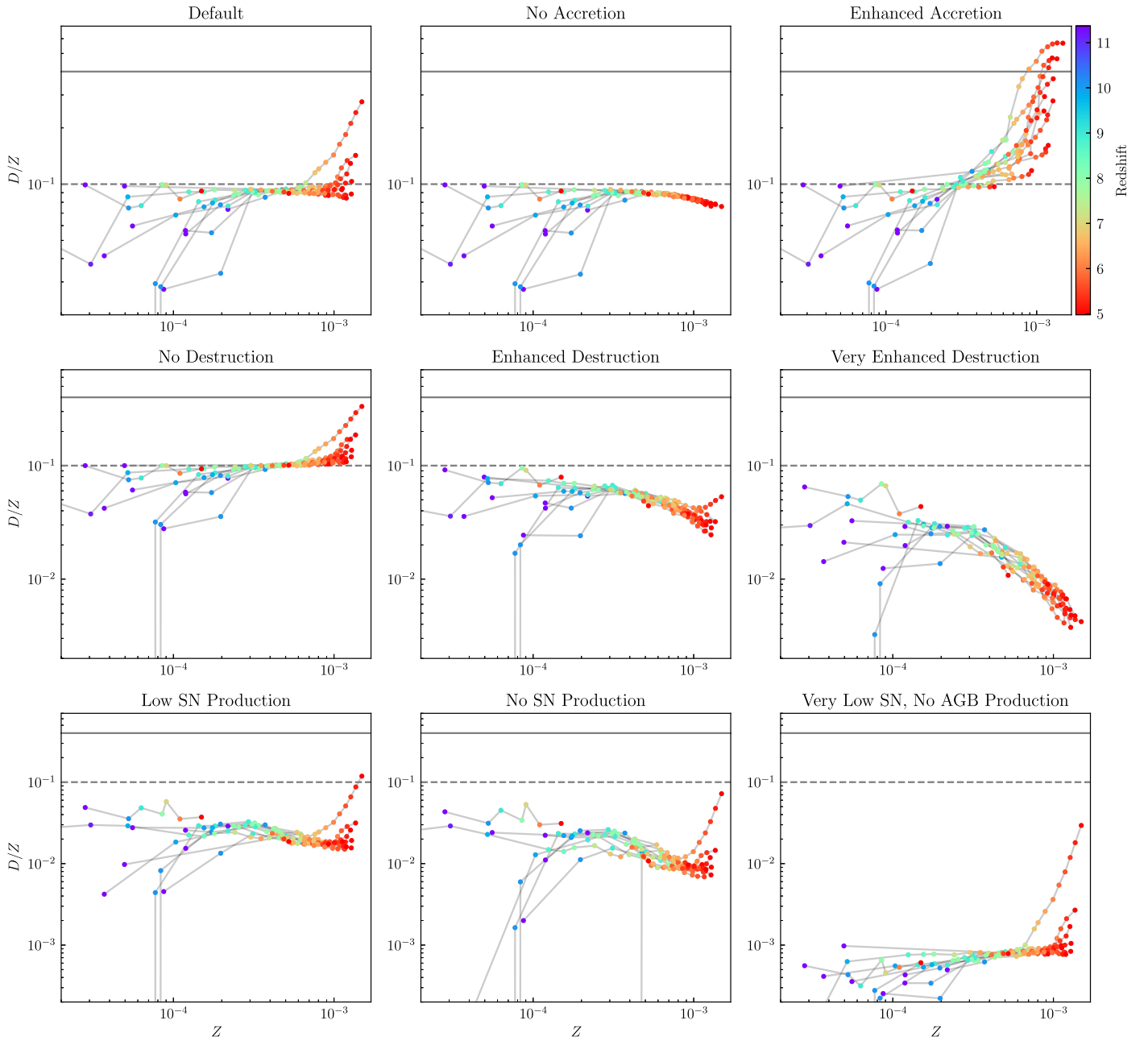


Figure 4. Galaxy-averaged D/Z vs. Z relations. Each panel shows the evolution of the dust content in our simulated galaxies with a different set of assumed dust model parameters, as indicated by the titles. Each point corresponds to the average D/Z and Z values for an individual galaxy at an individual snapshot. Z is in physical (i.e., mass fraction) units. Points from the same galaxy are connected with gray lines, and colors indicate redshift. The dashed horizontal gray line indicates $D/Z = 0.1$, which is the default production yield in our model, and the solid horizontal gray line indicates $D/Z = 0.4$, the value for the Milky Way and a common choice in post-processing analyses (see Section 4.2).

noise occurs at such low metallicities that its effect on the total dust mass, which is normalized by the metallicity, is minor and should not strongly impact our conclusions. Additionally, the existence of clear trends at late times/high metallicities indicates that the predictions are well resolved for the most massive galaxies, which are the most relevant for comparison to observational data.

In Figures 5 and 6 we examine the predicted dust masses of our simulated galaxies as a function of stellar mass at different redshifts for the different dust models. Figure 5 shows Default and models with variations in accretion and destruction rates (the first and second rows of Figure 4), while Figure 6 shows models with varied production yields (third row of Figure 4). In

all cases, the dust mass exhibits an approximately linear scaling with stellar mass, with varied normalization depending on assumed production yields and destruction efficiencies. This normalization spans 2 dex at a given stellar mass for the entire suite of models herein considered. There is also a general steepening of the relationship at higher masses ($M_* \sim 10^8 - 10^9 M_\odot$) in models where accretion becomes efficient. These relationships are sufficiently tight to be well distinguished between different models in principle, although there is significant degeneracy between yield and destruction rates—Very Enhanced Destruction and No SN Production predict very similar values, which the first achieves by destroying dust with high efficiency while the second produces little dust to begin

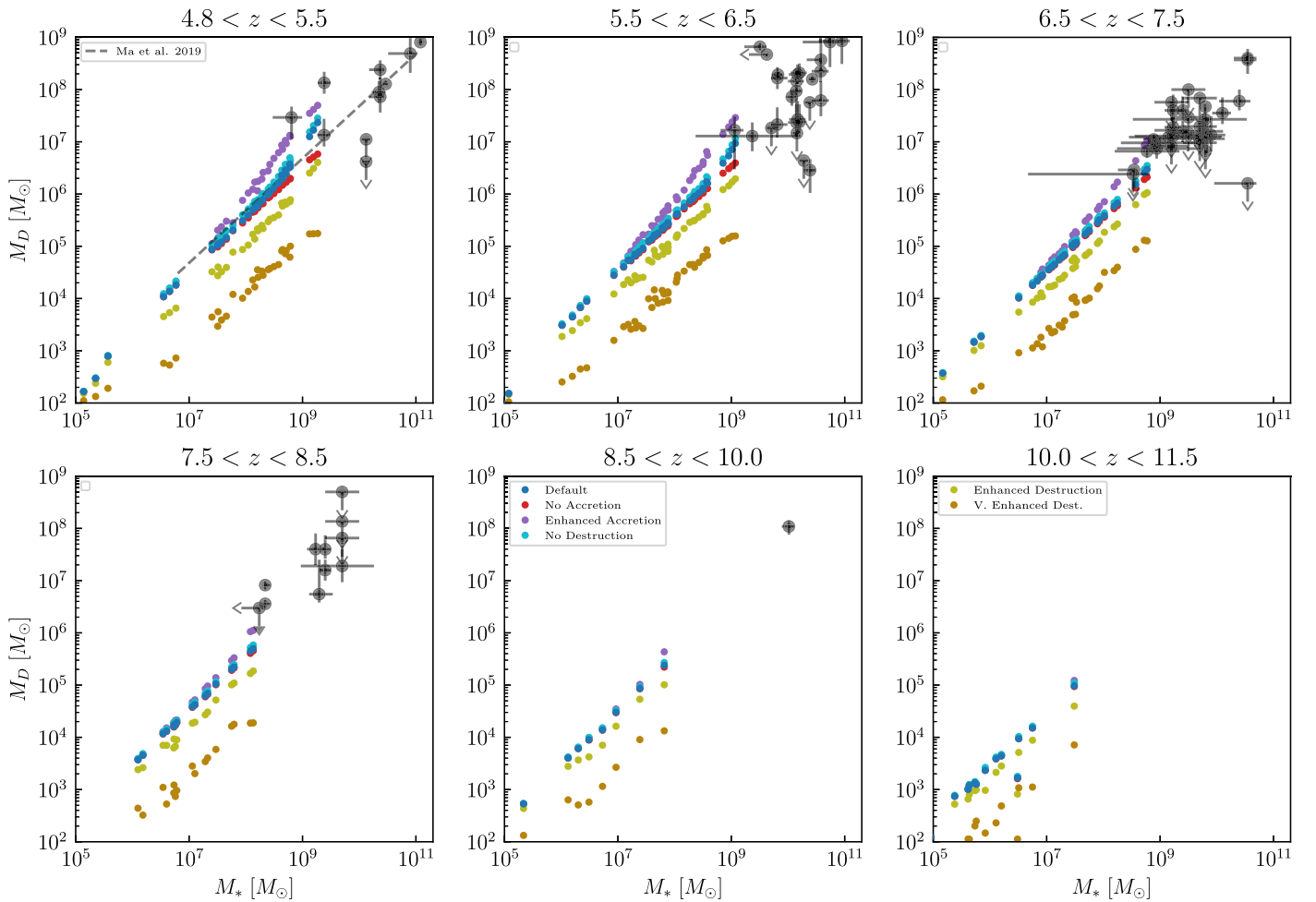


Figure 5. Dust mass–stellar mass relation. Colors indicate different dust models, which include Default and those with varied growth or destruction parameters (i.e., the first two rows of those shown in Figure 4). Each point is a single galaxy at a single redshift, and separate panels are redshift bins. Estimates based on observational data from Sommovigo et al. (2022), Dayal et al. (2022), Hashimoto et al. (2019), Knudsen et al. (2017), Schaerer et al. (2015), Watson et al. (2015), Laporte et al. (2017), Tamura et al. (2019), da Cunha et al. (2015), Marrone et al. (2018), Burgarella et al. (2020, with a redshift for ID27 from Aravena et al. 2016), Pozzi et al. (2021; also with stellar masses from Faisst et al. 2020), Witstok et al. (2023), and Leńniewska & Michałowski (2019; with a stellar mass from Ouchi et al. 2009) are shown with the same redshift binning. The predictions of a simpler dust post-processing model on higher-resolution simulations presented in Ma et al. (2019) are shown by the dashed gray line.

with. Additionally, models with the same yield but different growth timescales (Default, No Accretion, Enhanced Accretion) are only distinguishable at high masses and late times, consistent with the results of Figure 4. In summary, different plausible parameter choices for the dust model can change dust masses by up to two orders of magnitude at a given stellar mass. This flexibility highlights the need for a significant improvement in our understanding of dust production and destruction processes.

We therefore compare these predictions with existing observational estimates of dust masses in high-redshift galaxies from Sommovigo et al. (2022), Dayal et al. (2022), Hashimoto et al. (2019), Knudsen et al. (2017), Schaerer et al. (2015), Watson et al. (2015), Laporte et al. (2017), Tamura et al. (2019), da Cunha et al. (2015), Marrone et al. (2018), Burgarella et al. (2020; with a redshift for ID27 from Aravena et al. 2016), Pozzi et al. (2021; with stellar masses from Faisst et al. 2020), Witstok et al. (2023), and Leńniewska & Michałowski (2019). Because of the limited volume of our simulation, we do not capture unusually massive and therefore rare halos, limiting us to predictions at lower masses than almost all of the existing data. Nonetheless, the data appear to

favor those models with the highest dust masses—the data is always at the upper envelope of our simulation predictions wherever they overlap. Indeed, in both the $6.5 < z < 7.5$ and $7.5 < z < 8.5$ bins, most of the data appear to lie on or above the scaling relation of the most dust-rich model Enhanced Accretion if it were extrapolated. This suggests that the data prefer models in which production yields are high and ISM grain growth is efficient at high masses. We also note that the data appear to exhibit greater scatter at a given stellar mass than any one set of dust model parameters predicts.

However, we emphasize that these conclusions are extremely tentative because of the minimal amount of data available for comparison, the mostly disjoint stellar mass ranges probed by our simulations versus the observations, and especially the large systematic uncertainties in the observational constraints, which are not necessarily captured in the statistical uncertainties on quoted errors. Dust masses are derived from IR luminosities, which depend on dust mass, the dust extinction coefficient, and strongly on the dust temperature. The latter two are highly uncertain in high-redshift galaxies and difficult to independently constrain. In addition, our simulations may also miss some real sources of scatter, as we discuss further below.

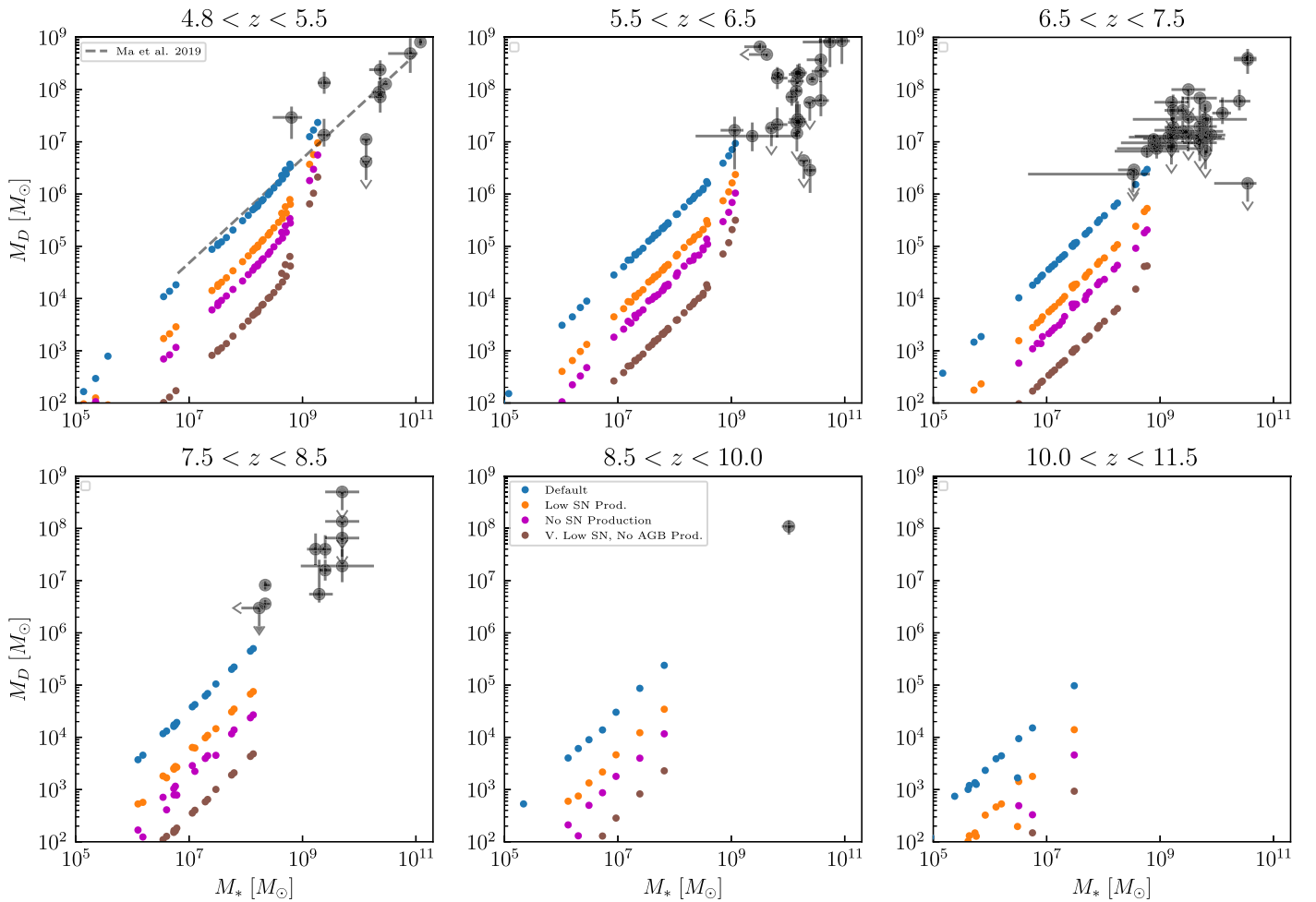


Figure 6. Dust mass–stellar mass relation (cont.). Same as Figure 5 but with Default and the dust models with varied yields (i.e., those in the third row shown in Figure 4).

Consequently, the most robust constraints will come from forward modeling of directly observable quantities.

3.3. Forward-modeled Observable Quantities: Comparison to Data

For the remainder of our analysis, we focus on a representative subset of the models discussed previously, each with a consistent color throughout the figures: Default (blue), Enhanced Accretion (purple), Enhanced Destruction (yellow), Very Enhanced Destruction (light brown), and Very Low SN, No AGB Production (dark brown).

3.3.1. Rest-frame UV Observables: M_{AB} , β_{UV} , τ_{1500}

Figure 7 compares the predicted UV spectral slopes of our simulated galaxies with these dust models to observational data. We also show the predictions of the simulations absent dust attenuation in black points. In contrast to the suggestions of Figures 5 and 6, the models with the lowest dust content—Very Enhanced Destruction, and Very Low SN, No AGB Production—agree best with the data, at all redshifts. It is not clear, however, if either model alone predicts as much scatter at a given luminosity as shown in the data.

In contrast, the more dust-rich models all predict similar β_{UV} values, which fail to overlap with the observations at any redshift, and exhibit large scatter. This is because they predict

very high ISM optical depths, as shown in Figure 8. For dust masses greater than or equal to those predicted by the Enhanced Destruction model, the dusty ISM is effectively opaque, so changes in dust content do not impact UV properties significantly. The spread in β_{UV} for these models is therefore likely due to the Poisson scatter in number of visible star particles along a given line of sight. Finally, we note that while the data prefer the dust-poor models, they are inconsistent with entirely dust-free predictions (black points), especially at later times.

3.3.2. Far-infrared Observables: IRX– β Relation, L_{IR}

In Figure 9 we examine the IRX– β relationships predicted by our modeling, compared to observational constraints. Because IR luminosity depends linearly on dust mass, models with distinctly different dust content are better separated in this parameter space. However, the predictions fail to match the data in two key ways: (1) No one model exhibits as much scatter as the observations, especially in the $5.5 < z < 6.5$ range, and (2) our simulations lack galaxies at low ($\lesssim 1$) IRX and high ($\gtrsim -1.5$) β_{UV} , which are apparent in the data.

Some of the reason for these disagreements is illuminated by examining the predictions in L_{IR} versus L_{UV} space, since these are the numerator and denominator of the IRX, respectively. This is shown in Figure 10, along with the same data as in Figure 9. While we predict reasonable L_{IR} especially at late

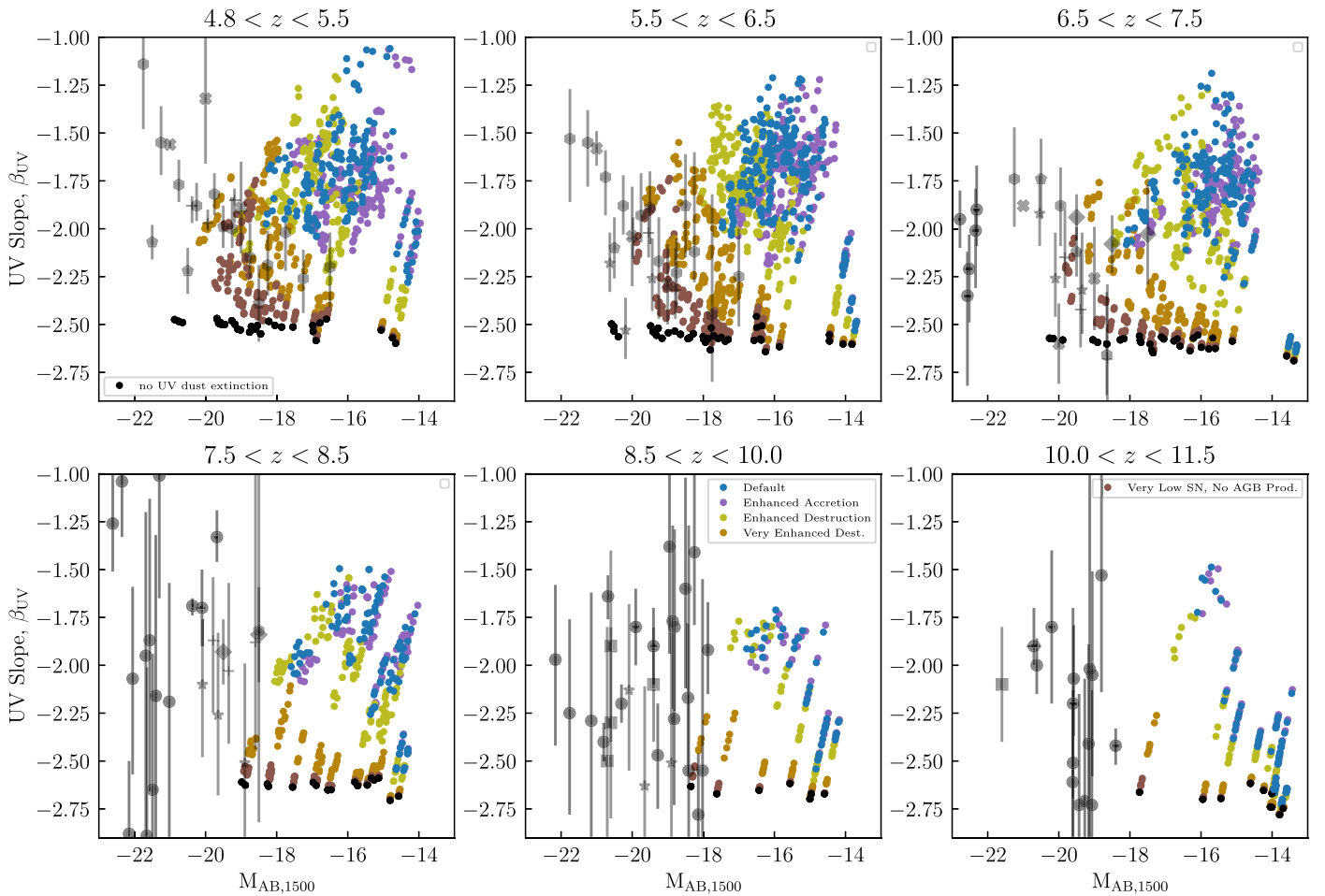


Figure 7. β_{UV} as a function of UV AB absolute magnitude. Different panels show data for different bins in redshift, different colors are different dust models, the black points indicate values predicted in the absence of dust, and the gray points are a compilation of observational measurements from the literature. Finkelstein et al. (2012, plus-signs), Bouwens et al. (2014, hexagons), Dunlop et al. (2013, diamonds), Bhatwadekar & Conselice (2021, stars), Wilkins et al. (2011, filled x), Dunlop et al. (2012, pentagons), and Wilkins et al. (2016, squares) show sample averages of multiple galaxies, while circles show measurements of individual galaxies with JWST from Roberts-Borsani et al. (2022), Naidu et al. (2022), Robertson et al. (2023), and Whittler et al. (2023), with both JWST and ground-based imaging results from Cullen et al. (2023), and with ground-based measurements from Bowler et al. (2022).

times, all of the galaxies in this observational sample exhibit higher UV luminosities than ours. This helps to explain the lack of low IRX galaxies in our predictions. This suggests that our models are predicting dust masses consistent with observations, but opacities that are too high, in agreement with the interpretations of Figures 5–7. Indeed, in Figure 10 we show the predictions of our simulations without dust attenuation as transparent points, and they are in better agreement with the data. This experiment is nonphysical in that the two luminosities are inconsistently calculated. However, it suggests that real galaxies have similar dust content to our more dust-rich models, but that it is distributed so as to have a much lower effective optical depth.

The inability of any one dust model to reproduce the scatter in observed IR luminosities could be due to our lack of self-consistently calculated dust temperatures—for simplicity and given the large modeling uncertainties involved, we assume a constant dust temperature of $T = 40$ K for these calculations (see Sommovigo et al. 2022). Since $L_{IR} \propto T_D^4$ at fixed M_D , galaxy–galaxy scatter in T_D could significantly enhance the predicted range of IRX. This limitation of our modeling is potentially the primary reason for the low scatter—dust temperatures depend on the radiation field, which, in turn, is

sensitive to short timescale variations in star formation rate. One therefore expects the ISM radiation fields, and consequently dust temperatures, to vary widely from galaxy to galaxy. Additionally, the lack of very massive galaxies in the limited cosmological volume of our simulation might also mean that we simply are not sampling galaxies as massive as those in existing observational samples, and this may also be the cause of one or both of these discrepancies to some degree.

It is of course also possible that the dust dynamical quantities assumed as inputs to each model, such as the characteristic time for dust grain growth in the ISM or the SN destruction efficiency—vary from galaxy to galaxy due to differences in ISM phase structure and dust content that our model is not sophisticated enough to capture. IR observables will therefore require significantly further theoretical efforts to be used as constraints on dust physics at high redshift.

3.4. Spatial Analysis

Figure 11 shows the predicted UV (1500 Å) emission, UV color β_{UV} , and dust column density (which is proportional to the IR emission) for different dust models. Consistent with the results of Section 3.3.1, all of our dust models predict significant extinction and reddening, but the amount and

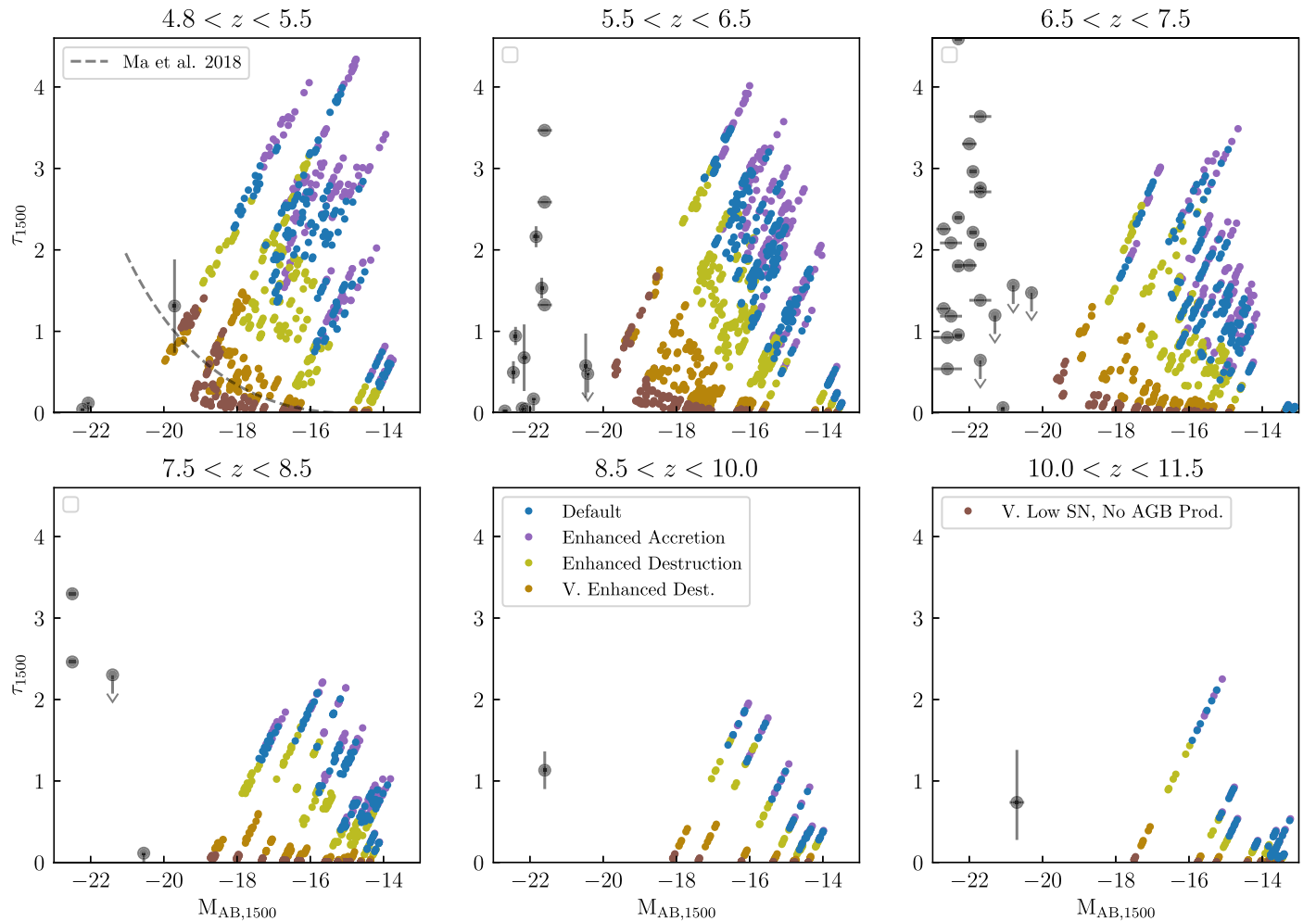


Figure 8. Dust optical depth in the UV vs. absolute UV magnitude. Observational upper constraints from Schaefer et al. (2015), Burgarella et al. (2020), Naidu et al. (2022), and Ferrara et al. (2022), with absolute UV magnitudes taken from Bouwens et al. (2022) are shown. In the lowest-redshift bin we also show the predictions from Ma et al. (2018) where high-resolution galaxy simulations were post-processed with a simpler dust model (see Section 4.2 for discussion).

spatial distribution vary markedly between the different models. The most dust-rich models show large amounts of reddening and extinction throughout the galactic disk, while those with less dust have effects that are more centrally concentrated. However, even those models with the least dust exhibit substantial attenuation and reddening in the center. This is because even the Very Enhanced Destruction model predicts dust column densities in excess of $\Sigma_D = 10^5 M_\odot \text{kpc}^{-2} \approx 10^{-5} \text{g cm}^{-2}$, which, for our assumed dust opacity of $\approx 10^5 \text{cm}^2 \text{g}^{-1}$ at 1500\AA , results in unity optical depth, and $\beta \gtrsim 0$ colors. The increasing severity of extinction at smaller projected galactocentric radii gives the UV emission a ring-like morphology in all but the least dusty model. Color is strongly correlated with IR emission though not perfectly; for example, both Default and Enhanced Accretion models exhibit the reddest colors in the disk outskirts/tidal tails, while the IR emission is highest in the center.

All but the Very Enhanced Destruction dust model show offsets in the location of maximum UV and IR emission on the order of 1 kpc for the same reason: the regions of highest IR emission are totally opaque to UV light. Note that this is despite the fact that the unattenuated UV light and dust are largely cospatial. Figure 12 shows the measured offsets in projected distance between locations of maximum UV and IR brightness for the same models, at all simulated redshifts,

sampling six lines of sight (positive and negative coordinate axes, which should be random with respect to the galaxy orientation) per snapshot. The top panels show these offsets as a function of absolute UV magnitude, on the bottom panels as a function of stellar mass. The leftmost panel of this figure is consistent with the trends noticed in Figure 11. Larger dust masses result in larger projected regions in which the dust is totally opaque to UV light. The maximum UV emission thereby happens at the larger projected radii where dust becomes optically thin, while the peak IR emission is always in the galactic center.

The middle and right panels show the results for the same images smoothed by a Gaussian beam of FWHM $0''.2$ and $0''.8$, respectively. The physical scale of the smoothing therefore depends on the snapshot redshift, and corresponds to 0.33 (1.32) kpc at $z = 11.4$ and 0.55 (2.19) kpc at $z = 5$ for an FWHM of 0.02 (0.08), respectively. The numbers were chosen to approximately match the resolutions of Hubble Space Telescope observations and ground-based (e.g., ALMA and UltraVISTA) observations, respectively. On the rightmost panel we show data from Inami et al. (2022) of UV-bright $z \sim 6-7$ galaxies for which dust continua was observed with ALMA and rest-frame UV (observation-frame near-IR) was observed as part of the UltraVISTA survey, both of which have approximately $0''.8$ FWHM resolution (McCracken et al. 2012).

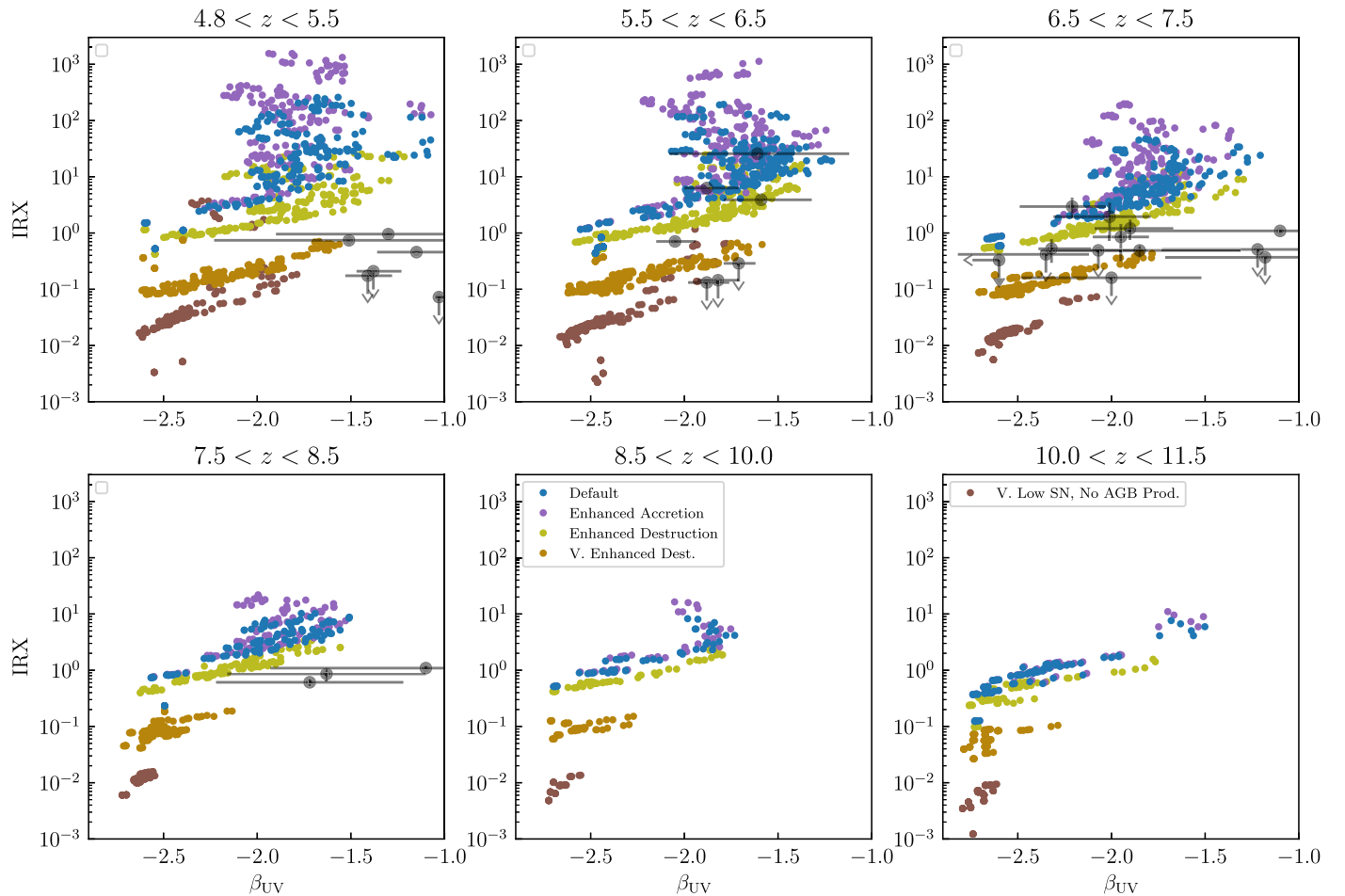


Figure 9. IRX– β_{UV} relation. Infrared-Excess (IRX) vs. ultraviolet spectral slope β_{UV} for our simulated galaxies in each dust model. Note that a constant dust temperature of $T_D = 40$ K was assumed in calculating all infrared luminosities. The colors and redshift bins are identical to Figure 7. Data shown are from Barisic et al. (2017; which includes data from Capak et al. 2015 and Pavese et al. 2016), the compilation from Hashimoto et al. (2019), and Bowler et al. (2022).

While these galaxies are clearly much brighter in the UV than ours, some exhibit very large UV-IR offsets that our simulated galaxy fails to exhibit when smoothed appropriately for comparison.

Indeed, we see that increased smoothing monotonically reduces the peak emission offset. Figure 13 demonstrates why: the angular symmetry of both the stellar and dust distributions results in a ring-like morphology of the UV emission at projected galactocentric distances where the dust becomes optically thin. While the offset of UV and IR maxima at infinite observational resolution is approximately the radius of this ring, at smoothing scales comparable to this radius, the UV light is maximized in the center, cospatial with the peak IR emission. The fact that this holds true for all sight lines in all snapshots for every dust model indicates that the UV-IR morphologies are similar in all cases. Peak UV and IR emission are never asymmetrically offset in a way that is preserved with degrading resolution. We have confirmed with a visual inspection of all snapshots that these conclusions are generic to our simulation at all relevant cosmological times. This generality leads us to strongly suspect that it would hold for higher-mass galaxies simulated with CROC physics and our dust model. This is especially the case since more massive galaxies would be expected to have greater dust masses.

4. Discussion

4.1. Status of Dust Constraints

We begin the discussion by assessing the success of our dust modeling efforts compared to current empirical constraints. There is no one model that appears to agree with all of the existing data. While the IR luminosities (and therefore estimated dust masses) appear to be best reproduced by models with comparatively higher dust content from high production yields and efficient growth, the models with the lowest dust content are in best agreement with β_{UV} constraints. We also note that none of our dust models individually reproduce the scatter in L_{IR} seen in observations. This could be due to the limited halo mass range of our simulation sample, the assumption of a fixed dust temperature for all galaxies (which, in reality, must depend on the ISM radiation field and the latter is expected to vary on short timescales and from galaxy to galaxy), the simplicity of our dust model, or some combination thereof. Together, these results suggest that while our model is capable of producing dust masses similar to those of real early-Universe galaxies, doing so results in UV opacities that are too high. We speculate that this could be due to the spatial distribution of dust relative to stars—that our galaxies are too uniform compared to the very turbulent ISM of real reionization-era galaxies, which we discuss in the context of our spatially resolved analysis below.

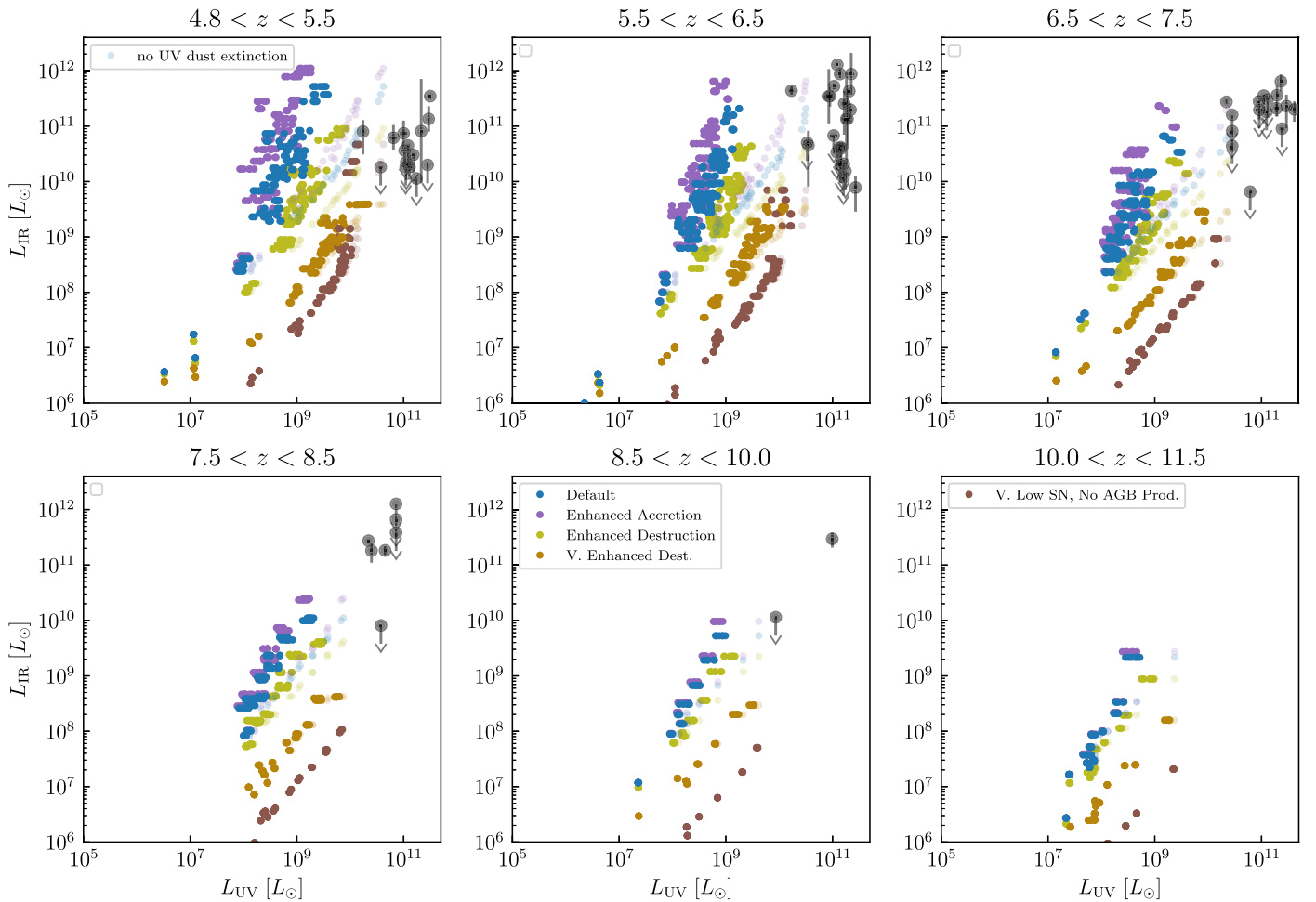


Figure 10. Infrared luminosity vs. UV luminosity. Colors and observational data are the same as Figure 9, with the addition of data from Burgarella et al. (2020). Additionally, we show predictions without UV dust attenuation in transparent points. These are inconsistent with the simulation, but show the effect of reduced UV opacity with unchanged dust mass.

We note that the observationally measured or derived quantities to which we compare are subject to significant systematic uncertainties, although we argue that these are likely not large enough to change our qualitative results. Even the calculation of β_{UV} values, which are in principle directly measurable from data, often requires assumptions because of the availability of only a few broadband wavelengths with low signal-to-noise detections. For example, Finkelstein et al. (2012), Bhatwadekar & Conselice (2021), Naidu et al. (2022), and Robertson et al. (2023) all reported β_{UV} values calculated from synthetic spectra corresponding to best-fitting model galaxy spectral energy distributions (SEDs). These require the assumption of a stellar population synthesis code (e.g., Bruzual & Charlot 2003), which can in principle impact the derived values (Reddy et al. 2018). The stellar masses quoted in Figures 3–5 are also constrained using galaxy SED modeling, which is subject to uncertainties in the properties of the assumed stellar population and dust attenuation (see Conroy 2013) and are likely on the order of ~ 0.5 dex (e.g., Faisst et al. 2020; Dayal et al. 2022). Metallicities in Figure 3 rely on various emission and absorption line measures, for one of which Jones et al. (2020) estimated a 0.4 dex systematic uncertainty. Dust masses calculated from a rest-frame IR continuum emission measurement at a single wavelength require the assumption of a dust temperature, which can be a

significant systematic uncertainty (see Figure 7 in Bakx et al. 2020). Nonetheless, the variety of observational methods and number of independent analyzes included in the compiled data to which we compare gives us hope that these systematic uncertainties are reflected in the spread of reported quantities and their associated error bars. Moreover, we believe they are unlikely to compensate for the very large discrepancies between observational constraints and our predictions, which constitute the central conclusion of our analysis.

We note also that the opacity law assumed for our calculation of observable quantities is another central uncertainty. As we do not evolve the full size distribution for the dust grains in our model nor their detailed chemical composition, we do not make predictions for how the dust optical properties in high-redshift galaxies may differ from those observed locally, and therefore simply assume a model for the lowest-metallicity system in the local Universe, where such properties have been well constrained (the “SMC bar” model of Weingartner & Draine 2001). Indeed, observations from JWST have indicated that the attenuation law in $z \sim 7$ –8 galaxies is both different from those measured at lower redshift and variable between galaxies (Markov et al. 2023). To test the effect of this uncertainty, we recalculated the observables used to make Figures 7–10 assuming instead the “Milky Way,

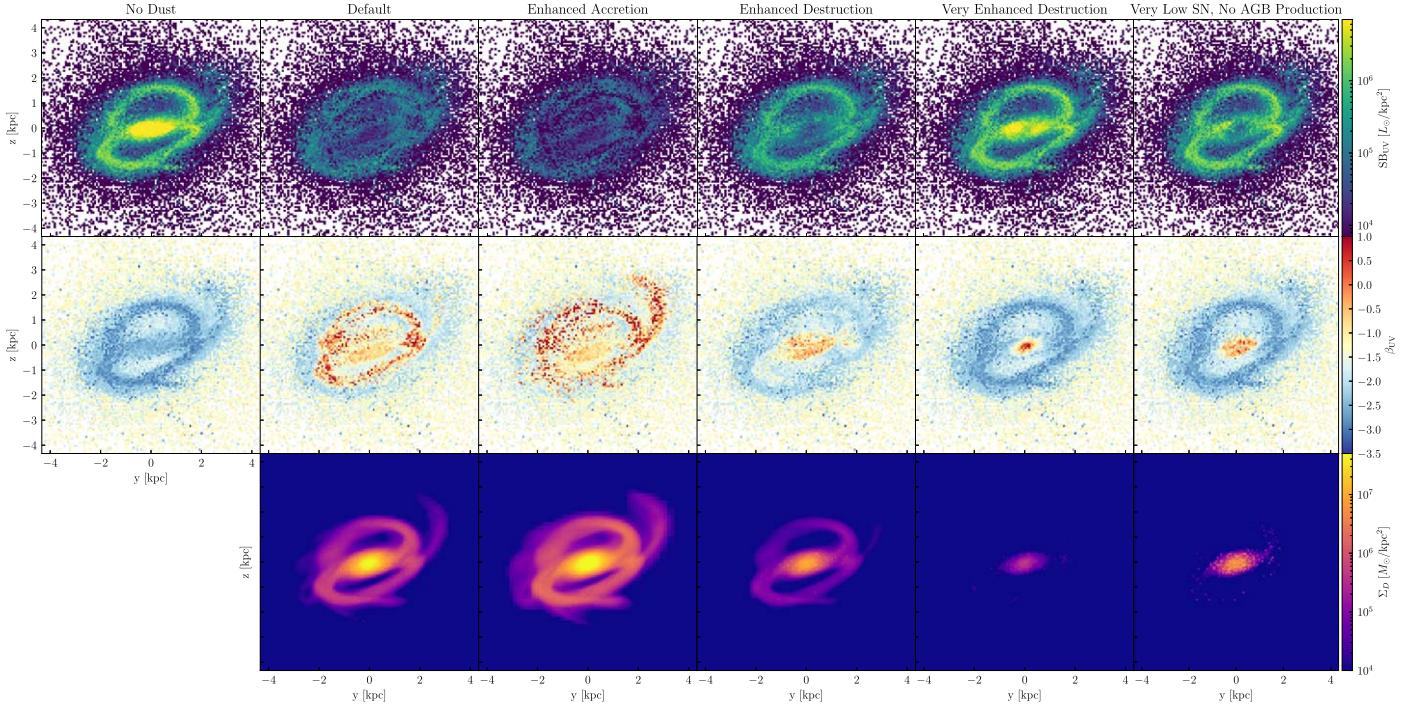


Figure 11. Images of the most massive galaxy in our box along a random line of sight at $z = 5$ with different dust models. The top row shows the 1500 \AA UV surface brightness, the middle row shows the spatially resolved UV beta slope (estimated using the 1500 and 2500 \AA color), and the bottom row shows the column density of dust mass (which is proportional to the IR surface brightness in the optically thin regime). Each column shows the predictions of a different set of dust model parameters, as well as the intrinsic UV emission on the leftmost column. Note that no smoothing has been applied to these images, and the pixelation is the result of the simulation grid.

$R_V = 3.1$ ” model from Weingartner & Draine (2001),⁶ and find that our predictions generally differ even more from observations, indicating that the SMC model optical properties we use by default are a best-case-scenario for our predictions (among existing well-characterized dust opacity laws), therefore strengthening our conclusion of irreconcilable disagreement between our forward-modeled predictions and observational constraints from real galaxies.

4.2. Comparison to Similar Theoretical Work

Lewis et al. (2023) recently presented results of an investigation with similar aims: they coupled an explicit model for dust very similar to ours to a galaxy formation simulation of cosmological reionization, and used this to predict the dust content and rest-frame UV observables of high-redshift galaxies. They presented predictions for a single choice of dust model parameters, in which they assume very low dust production yield $y_D = 10^{-3}$ and a much higher ISM growth accretion rate—they adopt a modestly shorter characteristic timescale (100 versus 300 Myr), and their expression has an additional factor of $1/Z \sim 10^3\text{--}10^4$. Consequently their galaxies transition from production-dominated to accretion-dominated dust content at a lower galaxy stellar mass of roughly $10^6 M_\odot$ in contrast to $\gtrsim 10^7 M_\odot$ in all of our models.

Their dust masses are therefore most similar to our highest-dust-content models. However, their model predicts much milder UV dust extinction than ours with similar dust masses (see their Figure 7). We speculate that this is due to differences in resolution: their maximum physical resolution is an order-of-

magnitude poorer than ours, at ~ 1 kpc. Given the observed sizes of high-redshift galaxies are $\lesssim 1$ kpc (Bouwens et al. 2020), their galaxies cannot possibly be spatially resolved and are therefore likely artificially large. This spreads the same amount of dust over a larger surface area and consequently reduces their predicted optical depths.

Graziani et al. (2020) and Di Cesare et al. (2023) also recently conducted simulations of high-redshift galaxies with a coupled dust physics model. Again, they only present predictions for a single set of dust model parameters, which appear to make qualitatively similar predictions between our Default and Enhanced Accretion models: Figure 4 of Graziani et al. (2020) indicates a production yield of $y_D \sim 0.1$, and a transition to accretion-dominated dust at $Z \sim 3 \times 10^{-2} Z_\odot \sim 6 \times 10^{-4}$. We note however that they adopt both a much shorter characteristic timescale for ISM accretion of 2 Myr to our 300 Myr, and a somewhat different accretion rate scaling of $dD/dt \propto DZ$ as opposed to our $dD/dt \propto D(f^{\text{dep}}Z - D)$. The two expressions tend to the same value at low D (modulo f^{dep} factor that is order-unity), but will differ significantly at higher D —while ours will tend to zero as $D \rightarrow Z$, corresponding physically to all of the available metals being locked in dust grains, and theirs increases unboundedly. This suggests that the plateau in D/Z at ≈ 0.4 with increasing Z exhibited by their model is due to enhanced destruction rates, which regulate the dust content, whereas in our model the transition is set by the $f^{\text{dep}}Z - D$ term in the growth rate going to zero.

Moreover, the fact that their model transitions to accretion-dominated at similar Z to ours despite a much higher growth-rate normalization suggests significant differences in the cold gas fractions or thermodynamics of the ISM in our simulations. We also note that their simulation accounts for dust dynamical effects at run time, which our post-processing model cannot.

⁶ Data obtained from https://www.astro.princeton.edu/~draine/dust/extcurvs/kext_albedo_WD_MW_3.1_60_D03.all.

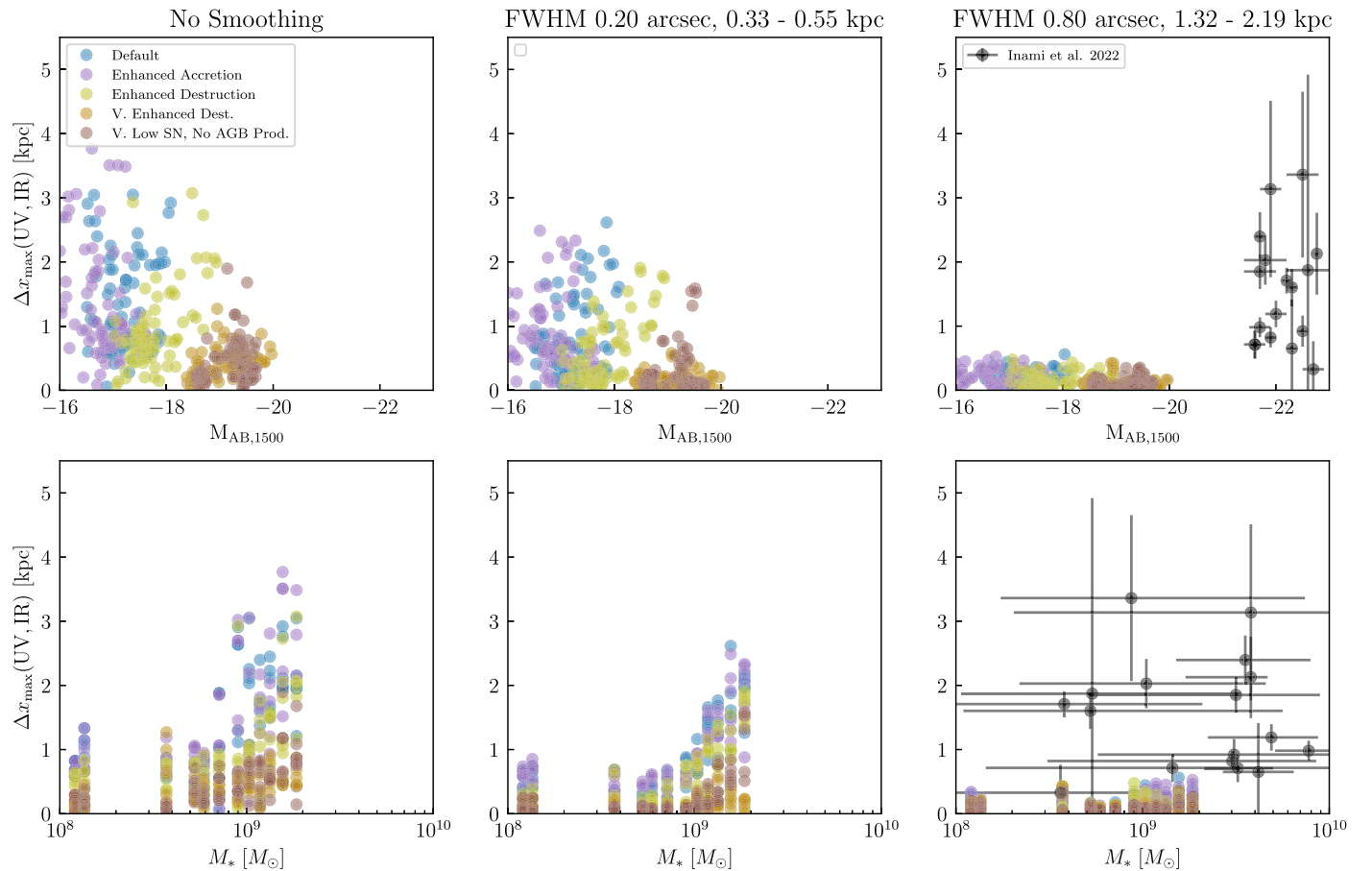


Figure 12. UV and IR peak emission offsets. The projected physical distance between the maximum UV emission (accounting for dust attenuation) and the maximum IR emission (as determined by the dust surface density), as a function of UV absolute magnitude (top row) and stellar mass (bottom row). Each point is one of six lines of sight for a each snapshot. Data for the most massive galaxy in our box at $5 < z < 8.5$ is shown. Different colors correspond to different dust models. Each panel shows different levels of smoothing to capture the effect of observational resolution. Data on the rightmost plot are from Table 4 of Inami et al. (2022; with stellar masses from Bouwens et al. 2022 and Schouws et al. 2022), whose observations have approximately $0''.8$ resolution in both the IR and UV (McCracken et al. 2012).

All of this suggests that (1) the predictions of these dust models are sensitive to the implementation details of cooling, star formation, and feedback in the ISM of high-redshift galaxies, and/or (2) that the back-reaction of dust dynamics on the ISM might be significant.

Lower et al. (2023b) simulated a suite of massive galaxies at high redshift with explicit dust physics based on the SIMBA galaxy formation model (Davé et al. 2019). Their dust model is also fully coupled to their galaxy formation physics during simulation run time, unlike ours, which is done in post-processing, but is otherwise very similar in physical processes accounted for and default parameters used. They simulate much more massive halos than we have in our limited simulation volume, and are therefore better able to directly compare to observational constraints on high-redshift dust masses. Their predictions broadly reproduce these observations, suggesting similar values to our most dust-rich models (as would be expected given the similarities of our models, particularly with our default parameters). However, they do not directly compare to measured rest-frame UV observables as we do, so it is unclear whether their models suffer from the same inability to simultaneously match stellar and dust emission constraints.

We also consider recent analyses that predict the dust content of high-redshift galaxies with simpler post-processing physical dust models, but with much higher-resolution (~ 10 pc) simulations that can more realistically resolve ISM dynamics

and phase structure. Ma et al. (2018, 2019) predicted dust-sensitive quantities from high-resolution simulations from the FIRE project (Hopkins & Squire 2018) of galaxies at $z \geq 5$ by assuming a constant $D/Z = 0.4$. While their analysis predict similar dust masses to our more dust-rich models (see the dashed gray line in Figure 5), their predicted effective optical depths are most consistent with our least dusty models (see Figure 8). Interestingly, this is also the case with the results from a similar study (Mushtaq et al. 2023) using the FirstLight simulation suite (Ceverino et al. 2017) and an identical dust post-processing model—see Figures 1 and 5 in Mushtaq et al. (2023).

FIRE and FirstLight are different galaxy formation simulations of similarly high resolution, both significantly higher than ours. Consequently, they better capture the effects of feedback on the high-redshift ISM, resulting in a more turbulent, porous gas distribution, which we speculate has a broader column density distribution than ours (see Figure 4 of Ma et al. 2019 and Figure 1 of Ceverino et al. 2021, both of which exhibit large gas column density fluctuations on scales smaller than our 100 pc resolution). This results in lower effective optical depths at a given dust mass because there exist low-density column channels through which UV radiation can escape that are lacking in our simulation.

Vijayan et al. (2022) adopted a post-processing method of intermediate sophistication to predict observables from

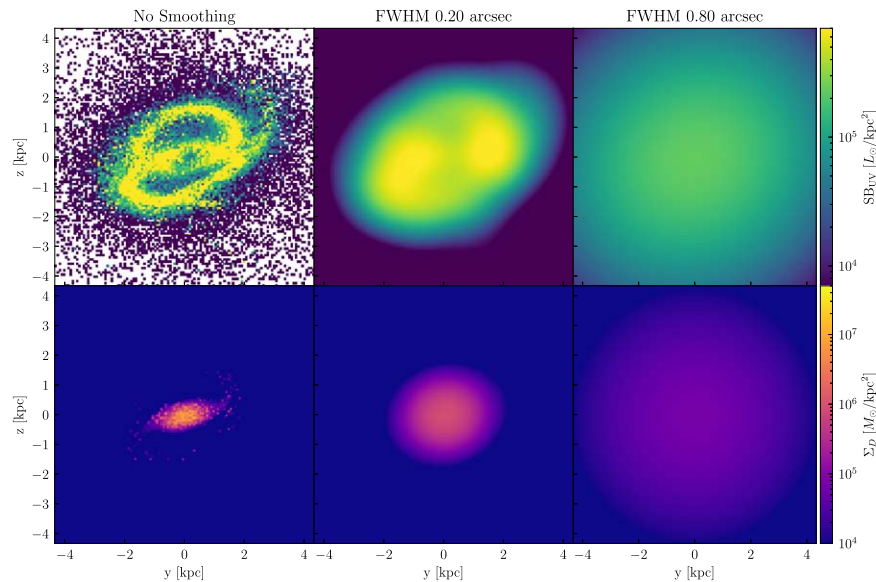


Figure 13. Effect of observation resolution on UV and IR morphologies.

simulations of high-redshift galaxies, specifically assuming an evolving dust-to-metal scaling relation from a dust physics prescription coupled to a different, semianalytical model of galaxy formation (Vijayan et al. 2019). Their assumed dust distributions are therefore not tied to the evolutionary histories of their individual simulated galaxies, but nonetheless trace the metals in a more realistic way than simply assuming a constant ratio. With D/Z values that appear to be similar to, but perhaps slightly lower than, our most dust-rich models (see their Figure 2), they appear to match the observed high-redshift $IRX-\beta_{UV}$ relation better than we do, despite similar simulation resolution. This may be because of differences in their galaxy model—they use the well-tested and successful EAGLE simulation physics (Schaye et al. 2015)—or because they calculated their IR luminosities by predicting the dust temperatures with radiative transfer post-processing, thereby accounting for the effect of different and evolving dust temperatures. This suggests that more careful calculation of dust temperatures may be important for matching observations with simulation predictions.

We have conducted an analysis of the predicted UV, IR, and UV color morphology of the most massive galaxy in our simulation under the assumption of different dust model parameters. We find that all models predict significant dust extinction in the central region of the galaxy, resulting in red $\beta_{\gtrsim -1}$ colors and in all but the model with the least dust ring-like morphology for the UV emission. This is because the dust contents predicted by our models are generally optically thick in a region that is approximately symmetrical about the galactic center, so the UV emission is dominated by the smallest radii at which dust becomes optically thin. Color is also strongly correlated with dust column, which we use as a proxy for IR emission.

Since IR emission peaks in the center of the galaxy, there are approximately kiloparsec-scale offsets between the points of maximal UV and IR surface brightness when “observed” with infinite resolution, but degrading image resolution on scales similar to existing observational capabilities causes the UV emission to peak in the center due to its symmetric distribution, resulting in no offset between peak brightness in UV and IR.

While existing observations only probe galaxies brighter in the UV than the most massive in our sample, they do exhibit much larger offsets that are suggestive of more complicated morphologies than the ones predicted by our modeling efforts (see Figure 2 of Bowler et al. 2022 and Figure 7 of Inami et al. 2022). Indeed, Figure 3 of Bowler et al. (2022) displays UV color gradients much less symmetric than any of those predicted by our dust modeling.

We note that the analysis of galaxy-averaged observable properties would lead us to expect that the distributions of UV and IR emission predicted by our models would be overly smooth and symmetrical, given our inability to simultaneously match observed dust masses and optical depths. We interpreted this as evidence that our simulations fail to reproduce a sufficiently dynamic ISM and consequently the full distribution of dust column densities, the lower tail of which could allow for significantly enhanced UV emission without decreased dust mass. The results of this spatially resolved analysis provide evidence in favor of this interpretation, given the inability of our modeling to reproduce the asymmetric morphologies seen in data of galaxies with similar stellar masses.

Simulation resolution and feedback prescription are the two most important numerical components of a fluid-dynamical galaxy formation model for determining the structure and dynamics of the ISM, and therefore one or both of these is likely implicated in our modeling failures. At a spatial resolution of 100 pc, our simulations do not resolve the disk scale-height and therefore cannot capture fully 3D phenomena that characterize the ISM phase structure like molecular clouds and SN feedback “super-bubbles.” As a consequence, the delayed cooling feedback prescription utilized in CROC appears to be incapable of driving large-scale galactic winds—we have watched movies of the tracer particles used in this analysis, and they are never removed from the galaxy ISM, indicating a negligible mass flux from the ISM into the circumgalactic medium. This is in stark contrast to most other modern galaxy formation models in which galaxies of the relevant mass range drive strongly mass-loaded winds, especially at early cosmological times (e.g., Muratov et al. 2015; Pandya et al. 2021). A feedback prescription that

successfully launches winds would reduce the gas mass and therefore dust mass in our galaxies, possibly reducing the high opacities of our most dust-rich models. These winds might also carve out low column density sight lines with minimal dust extinction.

Ma et al. (2018, 2019) and Liang et al. (2021) thoroughly explored the UV-to-IR observable properties of reionization-era galaxies predicted by the FIRE-2 simulations, which are significantly higher resolution than ours (~ 10 pc) and have been demonstrated to drive galactic winds. While they do not explicitly quantify any offsets between predicted UV and IR emission in their simulations, we see suggestions from their analysis of the dynamic, asymmetric ISM seen in observations and lacking in our simulations. Figure 4 of Ma et al. (2019) shows images of UV light and dust column density for two of their simulated galaxies, which both display a much more disturbed morphology than anything we find in our analysis. Close inspection reveals that the regions of brightest UV surface brightness correspond to holes in the dust surface density that appear to be blown out by strong feedback. However, we note that the spatial offsets between peak UV and IR emission do not visually appear to be much larger than 1 kpc, but firm conclusions cannot be drawn from images of just two galaxies each at a single snapshot. Figure 12 of Liang et al. (2021) did explicitly show a galaxy with >1 kpc offset between maximum UV and IR surface brightness, due to a highly perturbed and asymmetric distribution of gas with respect to stars (though we note that this galaxy is significantly more massive than those in our analysis). They also found that the effective UV optical depth does not correlate with dust mass at all at high redshift $z=6$ because of large variations in the star-dust geometry predicted by their simulations. All of this suggests that higher-resolution simulations with a feedback model that drives galactic winds may be better able to match the asymmetric UV/IR morphologies seen in observations.

The SERRA project is another suite of high-resolution cosmological simulations of galaxies at $z > 6$. These simulations are higher resolution than ours by about a factor of 3 with minimum cell sizes of ~ 30 pc, and consequently have different star formation and feedback prescriptions, more similar to those in FIRE-2 (Behrens et al. 2018; Pallottini et al. 2022). In contrast to our work and similar to FIRE, they found a clumpy morphology for both stars and dust, which, in some cases, leads to spatial offsets (Pallottini et al. 2022). They also found that this clumpiness results in low effective optical depths due to dust, although star-forming regions can locally exhibit very high optical depths (Behrens et al. 2018). It is interesting to note that Figure 4 of Behrens et al. (2018) does appear to exhibit a ring-like morphology in the galaxy’s central UV emission, suggesting this effect might persist to higher-resolution simulations. Nonetheless, the relative UV and IR properties of these galaxies are strongly influenced by the presence of dusty, star-forming clumps, which our simulations could not resolve, suggesting resolution is a main issue for our theoretical predictions.

Our results therefore provide strong motivation for the development of dust models, such as the ones presented here in higher-resolution simulations of galaxy formation with more realistic feedback. This results in a manifestly multiphase ISM, and appears to be essential to capturing the effects to which observations are most sensitive.

5. Conclusion

We apply the dust post-processing model described in Esmerian & Gnedin (2022) to a suite of 11 simulated galaxies from the CROC project. We explore nine different sets of dust parameters and quantify the effect of their variation on the dust content of high-redshift galaxies. We then forward model observable properties of high-redshift galaxies and compare to existing data. Our conclusions are as follows:



1. Comparing our simulated galaxies to a compilation of recent constraints on the metallicities of reionization-era systems, we find general agreement, although CROC might slightly underpredict metallicity at a given stellar mass.
2. We vary dust model parameters governing the rate of grain growth due to accretion in the ISM, the efficiency of grain destruction in SNRs, and the dust yields of production sources (SN and AGB star winds), to determine their impact on the predicted dust contents of high-redshift galaxies. We qualitatively validate the results of Esmerian & Gnedin (2022), in which we reproduced a well-established behavior of these dust models (see Hirashita 2013, for a review): the dust content of galaxies is set at early times/low metallicities primarily by the assumed production yields, while at higher metallicities/late times it is set by the competition between accretion and destruction, normalized by the initial condition set by production yields. The transition occurs around $Z \sim 2-4 \times 10^{-4} = 1-2 \times 10^{-2} Z_{\odot}$, with some dependence on assumed model parameters.
3. However, we observe significant scatter between galaxies at a constant metallicity, especially at late times/higher metallicities for models in which growth via accretion becomes efficient. This indicates the existence of important secondary dependencies beyond metallicity that determine the dust content of galaxies, which is not captured by typical one-zone models (e.g., Feldmann 2015). We speculate that this is driven by some combination of star formation history and ISM phase structure dependence, as is evidenced by the particularly aggressive growth via accretion in the most massive galaxy compared to the other galaxies in our sample.
4. We compare our total predicted dust masses as a function of stellar mass to observational constraints in the literature, and while our limited simulation size fails to sample galaxies as massive as most of those with observational constraints, where there is overlap we find our most dust-rich models—Default and Enhanced Accretion—appear to predict scaling relations consistent with current data. This suggests that the data prefer models in which production yields are high and ISM grain growth is efficient at high masses. The data also appear to exhibit larger scatter at a given stellar mass than predicted by any one of our models, but due to both large systematic uncertainties in the dust mass observational constraints and the disjoint range of stellar masses probed by our simulations versus the observations, these conclusions are tentative. Nevertheless, it is easy to imagine several additional sources of scatter that are missed in our simulations and post-processing, such as dependence of the dust temperature on the local radiation field or deficiency of the stellar feedback model.

5. We forward model directly observable galaxy properties from our simulations to make more direct comparison to data, and find that we are unable to simultaneously match existing observational constraints with any one model. Specifically, the models that best match the observed spectral slope in the UV, β_{UV} , are the models with the least amount of dust content due to either low production yields or very high destruction rates. However, these models fail to predict sufficiently high IR luminosities. Those that do predict IR luminosities consistent with observations have far too much dust attenuation and thereby fail to agree with β_{UV} constraints. Finally, we note that no one of our models appear to predict as much scatter in these observable quantities as the data exhibit.
6. We speculate that these deficiencies are due to issues with the spatial distribution of dust relative to stars in our simulations, which may be overly smooth. To assess this hypothesis, we compare our simulations to spatially resolved observations of rest-frame UV emission and dust continuum (Inami et al. 2022), between which some galaxies show large spatial offsets, indicative of a highly dynamic ISM. We compare data from galaxies of similar estimated stellar mass to our most massive system, and find that all of our models fail to predict offsets as large as observed, lending support to the idea that our galaxies fail to capture the dynamic complexity of the high-redshift ISM, which is necessary to reproduce observations.

Acknowledgments

This manuscript has been coauthored by Fermi Research Alliance, LLC under contract No. DE-AC02-07CH11359 with the U.S. Department of Energy, Office of Science, Office of High Energy Physics. This work used resources of the Argonne Leadership Computing Facility, which is a DOE Office of Science User Facility supported under contract DE-AC02-06CH11357. An award of computer time was provided by the Innovative and Novel Computational Impact on Theory and Experiment (INCITE) program. This research is also part of the Blue Waters sustained-petascale computing project, which is supported by the National Science Foundation (awards OCI-0725070 and ACI-1238993) and the state of Illinois. Blue Waters is a joint effort of the University of Illinois at Urbana-Champaign and its National Center for Supercomputing Applications. This manuscript is based upon work that is supported by the Visiting Scholars Award Program of the Universities Research Association. This work was completed in part with resources provided by the University of Chicago's Research Computing Center. Our analysis made use of the following publicly available software packages: Matplotlib (Hunter 2007), SciPy (Jones et al. 2001), NumPy (Walt et al. 2011), COLOSSUS (Diemer 2018), and yt (Turk et al. 2011). This manuscript is presented as part of a thesis to the Department of Astronomy and Astrophysics, the University of Chicago, in partial fulfillment of the requirements for the relevant Ph.D. degree. C.J.E. acknowledges support from the Knut and Alice Wallenberg Foundation through grant No. KAW 2020.0081.

ORCID iDs

Clarke J. Esmerian  <https://orcid.org/0000-0003-4575-4845>
 Nickolay Y. Gnedin  <https://orcid.org/0000-0001-5925-4580>

References

- Algera, H. S. B., Inami, H., Oesch, P. A., et al. 2023, *MNRAS*, 518, 6142
 Aravena, M., Decarli, R., Walter, F., et al. 2016, *ApJ*, 833, 71
 Arrabal Haro, P., Dickinson, M., Finkelstein, S. L., et al. 2023a, *Natur*, 622, 707
 Arrabal Haro, P., Dickinson, M., Finkelstein, S. L., et al. 2023b, *ApJL*, 951, 22
 Bakx, T. J. L. C., Tamura, Y., Hashimoto, T., et al. 2020, *MNRAS*, 493, 4294
 Barisic, I., Faisst, A. L., Capak, P. L., et al. 2017, *ApJ*, 845, 41
 Barrufet, L., Oesch, P. A., Bouwens, R., et al. 2023, *MNRAS*, 522, 3926
 Behrens, C., Pallottini, A., Ferrara, A., Gallerani, S., & Vallini, L. 2018, *MNRAS*, 477, 552
 Behroozi, P., Wechsler, R. H., Hearin, A. P., & Conroy, C. 2019, *MNRAS*, 488, 3143
 Bhatwadekar, R., & Conselice, C. J. 2021, *ApJ*, 909, 144
 Bianchi, S., & Schneider, R. 2007, *MNRAS*, 378, 973
 Bouwens, R., González-López, J., Aravena, M., et al. 2020, *ApJ*, 902, 112
 Bouwens, R., Illingworth, G., Oesch, P., et al. 2023, *MNRAS*, 523, 1009
 Bouwens, R. J., Illingworth, G. D., Oesch, P. A., et al. 2014, *ApJ*, 793, 115
 Bouwens, R. J., Smit, R., Schouws, S., et al. 2022, *ApJ*, 931, 160
 Bowler, R. A. A., Cullen, F., McLure, R. J., Dunlop, J. S., & Avison, A. 2022, *MNRAS*, 510, 5088
 Bruzual, G., & Charlot, S. 2003, *MNRAS*, 344, 1000
 Bunker, A. J., Saxena, A., Cameron, A. J., et al. 2023, *A&A*, 677, 88
 Burgarella, D., Nanni, A., Hirashita, H., et al. 2020, *A&A*, 637, A32
 Calzetti, D., Kinney, A. L., & Storchi-Bergmann, T. 1994, *ApJ*, 429, 582
 Capak, P. L., Carilli, C., Jones, G., et al. 2015, *Natur*, 522, 455
 Ceverino, D., Glover, S. C. O., & Klessen, R. S. 2017, *MNRAS*, 470, 2791
 Ceverino, D., Hirschmann, M., Klessen, R. S., et al. 2021, *MNRAS*, 504, 4472
 Conroy, C. 2013, *ARA&A*, 51, 393
 Conroy, C., & Gunn, J. E. 2010, *ApJ*, 712, 833
 Cullen, F., McLure, R. J., McLeod, D. J., et al. 2023, *MNRAS*, 520, 14
 Curtis-Lake, E., Carniani, S., Cameron, A., et al. 2023, *NatAs*, 7, 622
 da Cunha, E., Walter, F., Smail, I. R., et al. 2015, *ApJ*, 806, 110
 Davé, R., Anglés-Alcázar, D., Narayanan, D., et al. 2019, *MNRAS*, 486, 2827
 Dayal, P., Ferrara, A., Sommovigo, L., et al. 2022, *MNRAS*, 512, 989
 Dell'Agli, F., Valiante, R., Kamath, D., Ventura, P., & García-Hernández, D. A. 2019, *MNRAS*, 486, 4738
 Di Cesare, C., Graziani, L., Schneider, R., et al. 2023, *MNRAS*, 519, 4632
 Diemer, B. 2018, *ApJS*, 239, 35
 Draine, B. T. 1990, in ASP Conf. Ser. 12, The Evolution of the Interstellar Medium, ed. L. Blitz (San Francisco, CA: ASP), 193
 Dunlop, J. S., McLure, R. J., Robertson, B. E., et al. 2012, *MNRAS*, 420, 901
 Dunlop, J. S., Rogers, A. B., McLure, R. J., et al. 2013, *MNRAS*, 432, 3520
 Dwek, E. 1998, *ApJ*, 501, 643
 Esmerian, C. J., & Gnedin, N. Y. 2022, *ApJ*, 940, 74
 Faisst, A. L., Capak, P. L., Davidzon, I., et al. 2016, *ApJ*, 822, 29
 Faisst, A. L., Schaerer, D., Lemaux, B. C., et al. 2020, *ApJS*, 247, 61
 Feldmann, R. 2015, *MNRAS*, 449, 3274
 Ferrara, A., Pallottini, A., & Dayal, P. 2023, *MNRAS*, 522, 3986
 Ferrara, A., Sommovigo, L., Dayal, P., et al. 2022, *MNRAS*, 512, 58
 Ferrara, A., Viti, S., & Ceccarelli, C. 2016, *MNRAS*, 463, L112
 Finkelstein, S. L., Papovich, C., Salmon, B., et al. 2012, *ApJ*, 756, 164
 Fudamoto, Y., Oesch, P. A., Faisst, A., et al. 2020, *A&A*, 643, A4
 Gall, C., & Hjorth, J. 2018, *ApJ*, 868, 62
 Genel, S., Vogelsberger, M., Nelson, D., et al. 2013, *MNRAS*, 435, 1426
 Gjergo, E., Granato, G. L., Murante, G., et al. 2018, *MNRAS*, 479, 2588
 Gnat, O., & Sternberg, A. 2007, *ApJS*, 168, 213
 Gnedin, N. Y. 2014, *ApJ*, 793, 29
 Gnedin, N. Y. 2016, *ApJ*, 821, 50
 Gnedin, N. Y., & Draine, B. T. 2014, *ApJ*, 795, 37
 Gnedin, N. Y., & Kaurov, A. A. 2014, *ApJ*, 793, 30
 Graziani, L., Schneider, R., Ginolfi, M., et al. 2020, *MNRAS*, 494, 1071
 Hashimoto, T., Inoue, A. K., Mawatari, K., et al. 2019, *PASJ*, 71, 71
 Heintz, K. E., Brammer, G. B., Giménez-Arteaga, C., et al. 2023, *NatAs*, 7, 1517
 Hirashita, H. 2013, in Proc. Life Cycle of Dust in the Universe: Observations, ed. A. Andersen et al., 27
 Hopkins, P. F., & Squire, J. 2018, *MNRAS*, 479, 4681
 Hu, C.-Y., Zhukovska, S., Somerville, R. S., & Naab, T. 2019, *MNRAS*, 487, 3252
 Hunter, J. D. 2007, *CSE*, 9, 90
 Inami, H., Algera, H. S. B., Schouws, S., et al. 2022, *MNRAS*, 515, 3126
 Jones, E., Oliphant, T., Peterson, P., et al. 2001, SciPy: Open Source Scientific Tools for Python, <http://www.scipy.org/>
 Jones, T., Sanders, R., Roberts-Borsani, G., et al. 2020, *ApJ*, 903, 150
 Kirchsclager, F., Mattsson, L., & Gent, F. A. 2022, *MNRAS*, 509, 3218

- Knudsen, K. K., Watson, D., Frayer, D., et al. 2017, *MNRAS*, 466, 138
- Langeroodi, D., Hjorth, J., Chen, W., et al. 2023, *ApJ*, 957, 39
- Laporte, N., Ellis, R. S., Boone, F., et al. 2017, *ApJL*, 837, L21
- Le Fèvre, O., Béthermin, M., Faisst, A., et al. 2020, *A&A*, 643, A1
- Leśniewska, A., & Michałowski, M. J. 2019, *A&A*, 624, L13
- Lewis, J. S. W., Ocvirk, P., Dubois, Y., et al. 2023, *MNRAS*, 519, 5987
- Li, Q., Narayanan, D., & Davé, R. 2019, *MNRAS*, 490, 1425
- Liang, L., Feldmann, R., Hayward, C. C., et al. 2021, *MNRAS*, 502, 3210
- Lodders, K. 2019, arXiv:1912.00844
- Lower, S., Narayanan, D., Hu, C.-Y., & Privon, G. C. 2024, *ApJ*, 965, 123
- Lower, S., Narayanan, D., Li, Q., & Davé, R. 2023b, *ApJ*, 950, 94
- Ma, X., Hayward, C. C., Casey, C. M., et al. 2019, *MNRAS*, 487, 1844
- Ma, X., Hopkins, P. F., Garrison-Kimmel, S., et al. 2018, *MNRAS*, 478, 1694
- Markov, V., Gallerani, S., Pallottini, A., et al. 2023, *A&A*, 679, A12
- Marrone, D. P., Spilker, J. S., Hayward, C. C., et al. 2018, *Natur*, 553, 51
- Mason, C. A., Trenti, M., & Treu, T. 2023, *MNRAS*, 521, 497
- McCracken, H. J., Milvang-Jensen, B., Dunlop, J., et al. 2012, *A&A*, 544, A156
- McKee, C. 1989, in IAU Symp. 135, Interstellar Dust, ed. L. J. Allamandola & A. G. G. M. Tielens (Dordrecht: Kluwer), 431
- Micelotta, E. R., Dwek, E., & Slavin, J. D. 2016, *A&A*, 590, A65
- Michałowski, M. J., Hjorth, J., Gall, C., et al. 2019, *A&A*, 632, A43
- Mirocha, J., & Furlanetto, S. R. 2023, *MNRAS*, 519, 843
- Muratov, A. L., Kereš, D., Faucher-Giguère, C.-A., et al. 2015, *MNRAS*, 454, 2691
- Mushtaq, M., Ceverino, D., Klessen, R. S., Reissl, S., & Puttasiddappa, P. H. 2023, *MNRAS*, 525, 4976
- Naidu, R. P., Oesch, P. A., van Dokkum, P., et al. 2022, *ApJL*, 940, L14
- Nakajima, K., Ouchi, M., Isobe, Y., et al. 2023, *ApJS*, 269, 33
- Noel, I., Zhu, H., & Gnedin, N. 2022, arXiv:2210.16750
- Ouchi, M., Ono, Y., Egami, E., et al. 2009, *ApJ*, 696, 1164
- Pallottini, A., Ferrara, A., Gallerani, S., et al. 2022, *MNRAS*, 513, 5621
- Pandya, V., Fielding, D. B., Anglés-Alcázar, D., et al. 2021, *MNRAS*, 508, 2979
- Pavesi, R., Riechers, D. A., Capak, P. L., et al. 2016, *ApJ*, 832, 151
- Pillepich, A., Nelson, D., Springel, V., et al. 2019, *MNRAS*, 490, 3196
- Pozzi, F., Calura, F., Fudamoto, Y., et al. 2021, *A&A*, 653, A84
- Reddy, N. A., Oesch, P. A., Bouwens, R. J., et al. 2018, *ApJ*, 853, 56
- Roberts-Borsani, G., Morishita, T., Treu, T., et al. 2022, *ApJL*, 938, L13
- Roberts-Borsani, G., Treu, T., Chen, W., et al. 2023, *Natur*, 618, 480
- Robertson, B. E., Tacchella, S., Johnson, B. D., et al. 2023, *NatAs*, 7, 611
- Rodighiero, G., Bisigello, L., Iani, E., et al. 2023, *MNRAS*, 518, L19
- Schaerer, D., Boone, F., Zamojski, M., et al. 2015, *A&A*, 574, A19
- Schaye, J., Crain, R. A., Bower, R. G., et al. 2015, *MNRAS*, 446, 521
- Schneider, R., Valiante, R., Ventura, P., et al. 2014, *MNRAS*, 442, 1440
- Schouws, S., Stefanon, M., Bouwens, R., et al. 2022, *ApJ*, 928, 31
- Semenov, V. A., Kravtsov, A. V., & Gnedin, N. Y. 2018, *ApJ*, 861, 4
- Slavin, J. D., Dwek, E., Mac Low, M.-M., & Hill, A. S. 2020, *ApJ*, 902, 135
- Sommovigo, L., Ferrara, A., Pallottini, A., et al. 2022, *MNRAS*, 513, 3122
- Tacchella, S., Eisenstein, D. J., Hainline, K., et al. 2023, *ApJ*, 952, 74
- Tamura, Y., Mawatari, K., Hashimoto, T., et al. 2019, *ApJ*, 874, 27
- Tosi, S., Kamath, D., Dell'Agli, F., et al. 2023, *A&A*, 673, A41
- Turk, M. J., Smith, B. D., Oishi, J. S., et al. 2011, *ApJS*, 192, 9
- Valiante, R., Schneider, R., Bianchi, S., & Andersen, A. C. 2009, *MNRAS*, 397, 1661
- Vijayan, A. P., Clay, S. J., Thomas, P. A., et al. 2019, *MNRAS*, 489, 4072
- Vijayan, A. P., Wilkins, S. M., Lovell, C. C., et al. 2022, *MNRAS*, 511, 4999
- Vogelsberger, M., McKinnon, R., O'Neil, S., et al. 2019, *MNRAS*, 487, 4870
- Walt, S. v. d., Colbert, S. C., & Varoquaux, G. 2011, *CSE*, 13, 22
- Watson, D., Christensen, L., Knudsen, K. K., et al. 2015, *Natur*, 519, 327
- Weingartner, J. C., & Draine, B. T. 1999, *ApJ*, 517, 292
- Weingartner, J. C., & Draine, B. T. 2001, *ApJ*, 548, 296
- Whitler, L., Endsley, R., Stark, D. P., et al. 2023, *MNRAS*, 519, 157
- Wiersma, R. P. C., Schaye, J., & Smith, B. D. 2009, *MNRAS*, 393, 99
- Wilkins, S. M., Bouwens, R. J., Oesch, P. A., et al. 2016, *MNRAS*, 455, 659
- Wilkins, S. M., Bunker, A. J., Stanway, E., Lorenzoni, S., & Caruana, J. 2011, *MNRAS*, 417, 717
- Williams, H., Kelly, P. L., Chen, W., et al. 2023, *Sci*, 380, 416
- Witstok, J., Jones, G. C., Maiolino, R., Smit, R., & Schneider, R. 2023, *MNRAS*, 523, 3119
- Zhu, H., Avestruz, C., & Gnedin, N. Y. 2020, *ApJ*, 899, 137